Ore Geology Reviews 134 (2021) 104172

Contents lists available at ScienceDirect

Ore Geology Reviews

journal homepage: www.elsevier.com/locate/oregeorev

REE fractionation controlled by REE speciation during formation of the Renju regolith-hosted REE deposits in Guangdong Province, South China

Jian Huang [a,b], Wei Tan [a,b], Xiaoliang Liang [a,b], Hongping He [a,b,*], Lingya Ma [a,b], Zhiwei Bao [a,b], Jianxi Zhu [a,b]

[a] CAS Key Laboratory of Mineralogy and Metallogeny/Guangdong Provincial Key Laboratory of Mineral Physics and Materials, Guangzhou Institute of Geochemistry, Chinese Academy of Sciences, Guangzhou 510640, PR China
[b] University of Chinese Academy of Sciences, Beijing 100049, PR China

ARTICLE INFO

Keywords:
REE speciation
REE fractionation
Fe-Mn (hydr)oxides
Ion exchangeable fraction
Ce anomaly

ABSTRACT

Regolith-hosted rare earth element (REE) resources in South China are the dominant global source of heavy REEs (HREEs), which are critical for high technology and military industries. Most previous studies focused on the proportion of ion exchangeable REE fractions, but other speciations thereof and their effects on REE fractionation are still poorly understood. Therefore, to address this issue, this study focused on a systematic analysis of the geochemistry and mineralogy of a complete weathering 78 m profile in the Renju regolith-hosted REE deposit in northeast Guangdong Province, China. In the quartz diorite bedrock, the main REE minerals were titanite, allanite, and REE fluorocarbonates abundant in REEs (332–338 ppm). During the breakdown of rocks due to weathering, the light REE (LREE)-rich minerals, e.g., titanite and allanite, were dissolved preferentially, resulting in the release of the REEs. Thus, the HREE-rich minerals, including xenotime and zircon, are preserved with progressive weathering. The results of sequential extraction show that the activated REEs are immobilised, occurring mainly as ion exchangeable and Fe-Mn (hydr)oxide fractions, with a few amounts of the organic and carbonate binding fractions. Fe (hydr)oxides, as seen via transmission electron microscopy, usually occur in the form of goethite and hematite in the lower and upper parts of regoliths, respectively, while Mn is present as a trace element in Fe (hydr)oxides. The lower La/Yb ratios in the Fe-Mn (hydr)oxide fraction indicate that HREEs are preferably bonded on Fe-Mn (hydr)oxides, causing LREEs to exist mainly as ion exchangeable fractions. In addition, positive Ce anomalies exist in both the lateritic horizon with strong oxidation of weak acid and in the Fe-Mn (hydr)oxide fraction as a co-precipitate with Fe oxides. The results obtained advance our understanding of the mechanisms of REE fractionation and the mutual effect of REE speciation on the formation of regolith-hosted REE deposits in South China.

1. Introduction

Rare earth elements (REEs) consist of lanthanide elements from La to Lu and Y and can be divided into light rare earth elements (LREEs; La–Eu) and heavy rare earth elements (HREEs; Gd–Lu and Y). Given the increasing importance of renewable energy and high-technology applications, REEs–particularly the more scarce but important HREEs (Borst et al., 2020; Li and Zhou, 2020; Xu et al., 2017)– have been recognised as strategic resources and critical metals. Regolith-hosted REE deposits, also referred to as 'ion-adsorption REE deposits', currently contribute to ca. 15% of REE production worldwide (Li et al., 2020) and more than 90% of the global HREE supply (Riesgo Garcia et al., 2017).

Most regolith-hosted REE deposits are formed via intensive weathering of REE-rich Caledonian and Yanshanian granitoid or volcanic rocks (Li et al., 2017b; Sanematsu et al., 2016). In tropical and subtropical regimes, rock-forming minerals and primary REE-bearing minerals are decomposed with the release of REEs. Strong REE leaching occurs in the uppermost laterite of the weathering profile; otherwise, REEs accumulate as secondary REE minerals in the lower part of the regolith (Berger et al., 2014; Lara et al., 2018) or through adsorption on clay minerals (Li and Zhou, 2020; Yusoff et al., 2013) and Fe-Mn (hydr) oxides (Braun et al., 2018; Duzgoren-Aydin and Aydin, 2009). REE

* Corresponding author at: CAS Key Laboratory of Mineralogy and Metallogeny/Guangdong Provincial Key Laboratory of Mineral Physics and Materials, Guangzhou Institute of Geochemistry, Chinese Academy of Sciences, Guangzhou 510640, PR China.
E-mail address: hehp@gig.ac.cn (H. He).

https://doi.org/10.1016/j.oregeorev.2021.104172
Received 16 November 2020; Received in revised form 18 March 2021; Accepted 13 April 2021
Available online 20 April 2021

fractionation occurs through the dissolution of REE-bearing minerals (Harlavan and Erel, 2002; Sanematsu et al., 2016), formation of secondary REE-bearing minerals (Berger et al., 2008, 2014), complexation into organic and inorganic ligands (Davranche et al., 2004; Tang and Johannesson, 2010), scavenging by minerals via adsorption (Piasecki and Sverjensky, 2008; Yang et al., 2019), surface precipitation (Dardenne et al., 2002), and redox reactions (Janots et al., 2015). Most previous studies have focused mainly on the fractionation characteristics of ion-exchangeable REEs (Li et al., 2019; Sanematsu et al., 2013; Sanematsu and Watanabe, 2016; Yang et al., 2019). Although it has widely been accepted that regolith-hosted REE deposits contain 50% to 90% ion-exchangeable REEs, predominantly on the surface of kaolinite and halloysite (Li et al., 2017b; Sanematsu and Watanabe, 2016)–and that ion-exchangeable REEs mainly occur in the REE enrichment zone–the REE fractionation of the ion exchangeable fraction is not clearly understood at present. Sanematsu et al. (2013) found that the ion-adsorption fraction tends to be rich LREEs, when compared with whole-rock REE distribution of weathered granite, during the process of adsorption. However, simulations suggest that REE adsorption on kaolinite and halloysite through ion exchange shows only weak fractionation in weathering crust, i.e. when ionic strength and pH value are low (Coppin et al., 2002; Yang et al., 2019).

Recent studies have shown that apart from the ion exchangeable fraction, REEs also exist as fractions of Fe-Mn (hydr)oxides, organic and carbonate bindings, and residues (Fu et al., 2019; Li et al., 2019). Among the most important colloids in weathered crust of various rocks, Fe-Mn (hydr)oxides have particularly large surface areas; these control the concentration and transport of REEs in natural hydro-systems (Liu et al., 2017; Yu et al., 2017). The most widespread Fe (hydr)oxides, hematite and goethite, have a strong chemical affinity and stable structure that make them potentially attenuate REEs via adsorption, isomorphous substitution, and co-precipitation (Bolanz et al., 2018; Li et al., 2017a; Zhong et al., 2019). However, the contribution of the Fe-Mn (hydr)oxide fraction to the total REE concentration in weathering crust is often neglected owing to the relatively low REE proportions therein (Fu et al., 2019; Li et al., 2017b; Sanematsu et al., 2013). The chondrite-normalised Fe-Mn (hydr)oxide fractions are slightly enriched in HREEs (Li et al., 2019) and may play an important role redistributing HREEs in the weathering crust. In addition, the REE fractionation of the organic binding and carbonate binding fractions in the regolith-hosted HREE deposits remain poorly known, although few simulation experiments conducted indicate that organic matter and (bi)carbonate may be the mechanisms by which REEs are transported (Pourret et al., 2007a; Tang and Johannesson, 2010).

Sequential extraction is a typical method for classifying and extracting one or more substances from samples based on the physical properties (e.g. particle size and solubility) and chemical properties (e.g. binding state and reactivity) of the extracted states. Considering the difficulty of directly observing REE speciations via electron microscopy (e.g. scanning electron microscopy (SEM) and transmission electron microscopy (TEM)), sequential extraction may be a potential method to analyse the characteristics of REE fractionation because it allows easy and systematic extraction of REEs with different fractions in weathering crust. In this study, a complete and representative profile of regolith-hosted REE deposits was examined from the Renju mining area of Guangdong Province for detailed mineralogical and geochemical

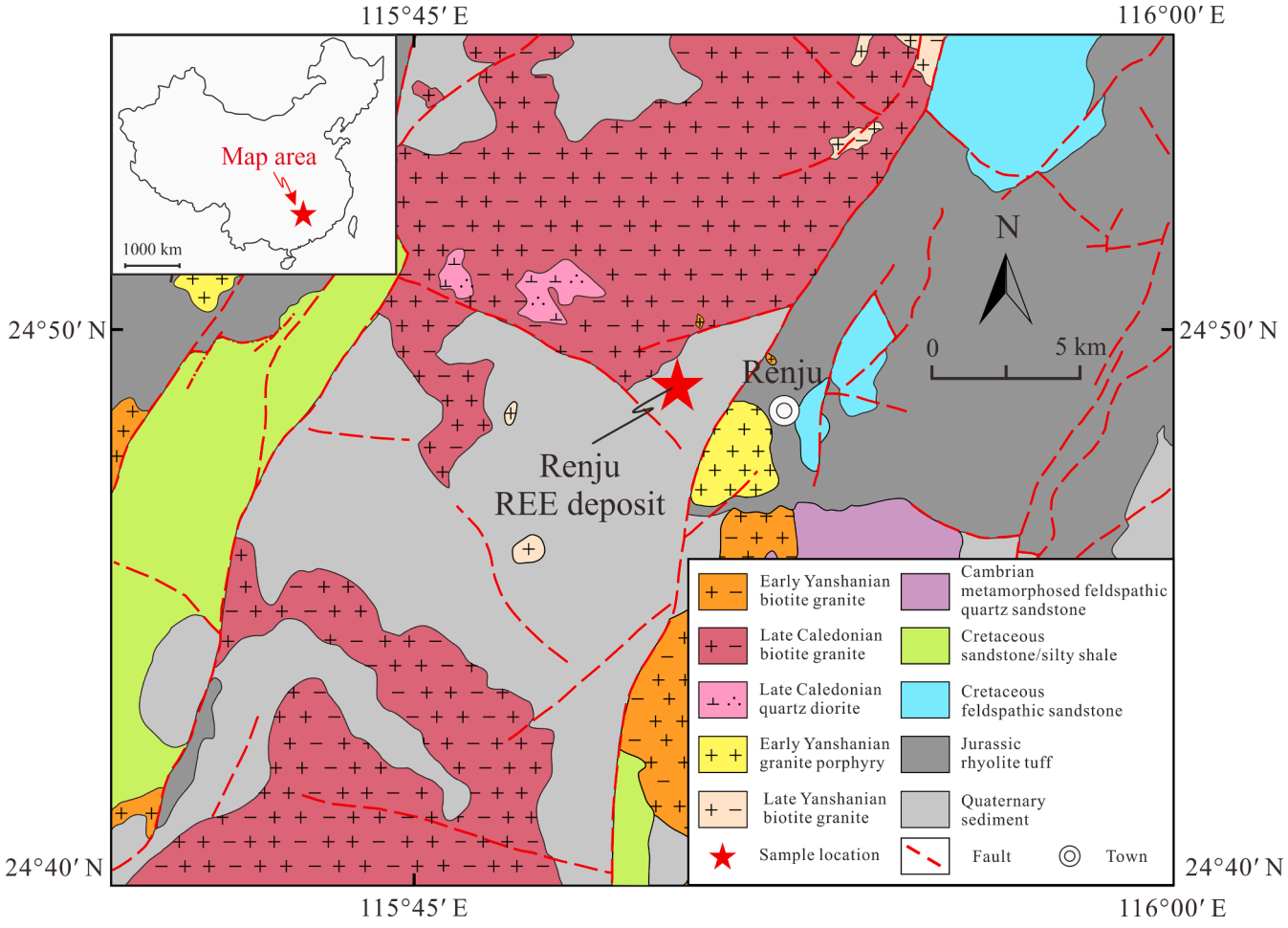

Fig. 1. Simplified geological map of the Renju rare earth mining area (after Regional Geological Survey Team of Jiangxi Geological Bureau, 1976).

analyses. The distribution of REEs was analysed via sequential extraction. This study attempts to clarify the speciation of REEs and their fractionation mechanism in regolith-hosted REE deposits in South China and to provide a basis for the exploitation and efficient utilisation of such deposits.

2. Geologic background

The Renju REE deposit is located in Renju town, Meizhou city, northeast Guangdong Province (Fig. 1). It currently has total 20,467 tonnes (t) of rare earth oxides (REOs) resources with an average grade of 0.172 wt % REOs (Wang and Xu, 2016). The deposit is hosted in the weathered crust of the Renju pluton, an early Yanshanian granitoid pluton with an exposed area of 29.3 km^2. The frequent magmatic activities made the metallogenic rocks mostly occurred in the form of small rock strains, such as Zuxitang, Huangniqu and Shenbei (Chen and Yu, 1994).

The Renju pluton consist of biotite granites, granite porphyries, and quartz diorites. NE- and NW-trending faults are mainly developed in this mining area (Fig. 1). Small quantities of Quaternary, Cretaceous, and Cambrian sediments and Yanshanian rhyolite tuff are exposed in the Renju area. The Renju regolith-hosted REE deposit is mainly developed in the weathered crust of the biotite granites. The distribution of the orebody is primarily controlled by the topography of the pluton, which are crescent-shaped lenses with an average thickness of 5.6 m.

A drill core was taken from the granite weathering profile in the Renju mining area (24°59′5″ N; 115°50′23.6″ E). The bedrock is fine-grained and equigranular quartz diorite (with a grain size of 0.5–2.0 mm) consisting of plagioclase (ca. 53%), amphibole (ca. 14%), biotite (ca. 10%), chlorite (the hydrothermally altered products of amphibole and biotite; ca. 10%), quartz (ca. 10%), and K-feldspar (ca. 4%). Accessory minerals include titanite, ilmenite, magnetite, zircon, allanite, apatite, monazite, and xenotime (Fig. 2). The terrain is dominated by a small (35 m) hill with a <25° slope; it is covered by grassy vegetation and a few trees and has elevation varying from 250 to 350 m above sea level. The climate in this region is subtropical and influenced by the East Asian monsoon (Chen et al., 2009), with an annual average temperature of approximately 25 °C and rainfall of 1500–2000 mm (Yang et al., 2019). The perennial wet and warm climate provides ideal conditions for intense chemical weathering.

3. Sampling and analytical methods

The samples studied were taken from a drill core extracted using a custom-made double-tube drilling system consisting of a stainless steel outer tube with a diamond drill bit and an PVC inner tube. The core was collected in the inner tube at intervals of 1.0 m as the drilling advanced. A 78.0 m long drill core of the entire weathering profile was obtained from laterite to fresh quartz diorite (Fig. 2).

3.1. Pre-treatment of the samples

After scraping off the outermost part of each sample in the drill core,

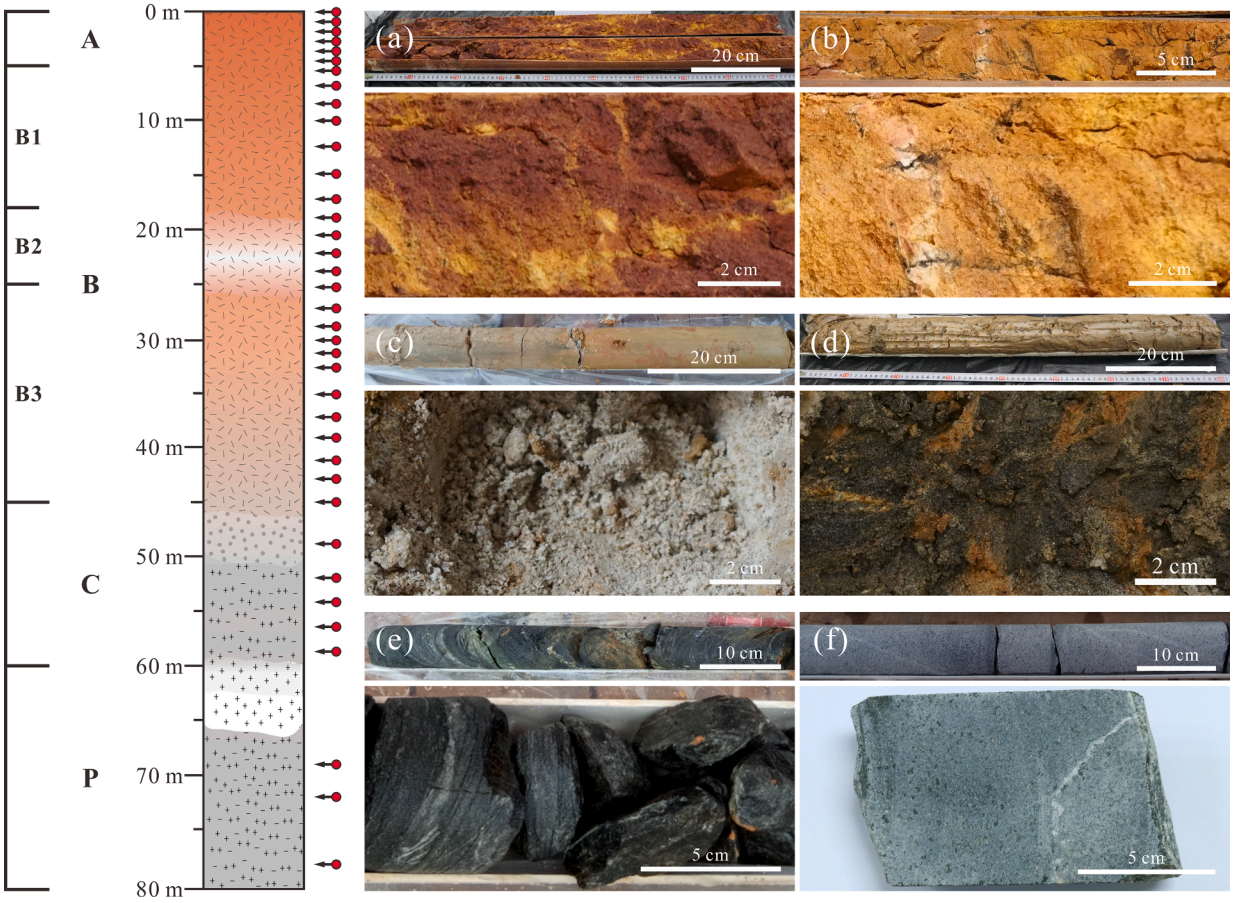

Fig. 2. Schematic of the weathering profile of the Renju deposit and photographs of the corresponding weathering stages. (a) Brownish red and yellow A horizon; (b) Yellow-mottled white B1 horizon; (c) White B2 horizon with abundant quartz and feldspar grains; (d) Brownish black-mottled yellow B3 horizon; (e) Greyish-green C horizon, appearing in this manner due to abundant biotite and hornblende chloritisation that preserves plutonic structures with the exception of oriented cracks; (f) Fresh bedrock with feldspar, quartz, amphibole, and biotite as major minerals.

uncontaminated samples from different weathering stages were collected at interval of 0.5 m for the first 2.0 m of the lateritic horizon and then at interval of 2.0 m for the rest of profile. A total of 38 samples were obtained. These samples were dried at 40 °C, ground into fine powder using a rotary disk mill, and selected for mineral composition, major/trace elements and REE speciation analyses. In addition, resin-impregnated polished thin sections were prepared using 20 samples collected from the bedrock to the lateritic horizon to allow REE mineral characterisation via SEM and with an electron probe micro-analyser (EPMA).

3.2. Mineral composition

Mineral compositions of the samples were measured on a Bruker D8 Advance X-ray diffractometer (XRD) between 3° and 80° (2θ) at a scanning speed of 3° min^{-1} with Cu Kα radiation (40 mA and 40 kV). Backscattered electron (BSE) images were obtained using a Hitachi SU8010 SEM equipped with an energy dispersive X-ray spectrograph at 15 kV. TEM and high-resolution TEM (HRTEM) images were obtained using a FEI Talos F200S instrument operating at 200 kV. The chemical compositions of the samples were analysed using a JEOL JXA-8230 EPMA at 15 kV and 20 nA.

3.3. Major element analysis

Before analysis, all the samples were calcined at 900 °C for 90 min to remove organic matter and carbonate. After this, approximately 0.50 g of each treated sample was weighed, mixed with 4.00 g $Li_2B_4O_7$, and fused into glass discs at 1200 °C. The major elements were measured from the glass discs using a Rigaku ZSX100e X-ray fluorescence spectrometer (Ramsey et al., 1995). The analytical precision of the major element content was better than 1% (relative standard deviation; RSD). The results of the major element analyses are given in Table A2.

3.4. Trace element analysis

The bulk samples from the drill core and the corresponding extracted residues were dried at 105 °C for 3 h and then baked at 550 °C for 3 h to eliminate organic material. Following this, approximately 0.04 g of each solid sample was analysed for trace elements using a Thermo Icap Qc inductively coupled plasma-mass spectrometer (ICP-MS) (Wang et al., 2018). Rh was added to each sample as an internal standard to calibrate the drift of the instrument during the measurements. The analytical precision for the trace element content was better than 3% RSD. Several United States Geological Survey and Chinese rock and sediment standards (GSR-2, GSR-3, GSD-09, GSD-11, SARM-4, W-2, and AGV-2) were used for external quality control. The results of the trace element analyses are given in Table A3.

3.5. Sequential extraction procedure

A seven-step sequential extraction routine was utilised to quantify different speciations of REEs in the Renju weathering profile (GBW07441-074451, 2007; Shi et al., 2014). The details of the step-extraction method for particular types of REEs are as follows:

(I) *Water-soluble REEs*. 1.00 g of bulk sample was immersed in 25 mL of ultrapure water (pH = 7 ± 0.2) in Teflon centrifuge tubes. The centrifuge tubes were shaken at room temperature (25 ± 0.2 °C) for 2 h. Following this, the supernatant was collected and the quantity of REEs was determined.

(II) *Ion-exchangeable REEs*. 25 mL of 1.0 mol L^{-1} MgCl solution (pH = 7 ± 0.2) was added to the residue. The centrifuge tubes were then shaken at room temperature (25 ± 0.2 °C) for 2 h, after which the supernatant was collected for REE quantity analysis.

(III) *Carbonate-binding REEs*. 25 mL of 1.0 mol L^{-1} CH_3COONa solution (pH = 5 ± 0.2) was added to the residue. The centrifuge tubes were shaken at room temperature (25 ± 0.2 °C) for 5 h. After centrifugation, the supernatant was collected to allow the determination of the REE concentration.

(IV) *Humic acid-binding REEs*. 35 mL of 0.1 mol L^{-1} $Na_4P_2O_7$ solution (pH = 10 ± 0.2) was added to the residue. The centrifuge tubes were shaken at room temperature (25 ± 0.2 °C) for 3 h. Following this, the supernatant was collected for analysis of the REE concentration.

(V) *REEs associated with Fe-Mn (hydr)oxides*. 35 mL of 0.25 mol L^{-1} NH_2OH–HCl solution (pH = 2 ± 0.2) was added to the residue. The centrifuge tubes were shaken at room temperature (25 ± 0.2 °C) for 6 h. The supernatant was then collected the analysis of the REE concentration.

(VI) *REEs associated with organic material*. 30% H_2O_2 and 0.02 mol L^{-1} HNO_3 were added to the residue. The tubes were shaken for 3 h in a hot water bath shaker at 85 °C. During this period, approximately 10 mL of 30% H_2O_2 in 0.02 mol L^{-1} HNO_3 (in total) was added to the residue in the centrifuge tubes 5 times every 30 min. The supernatant was collected after centrifugation to allow determination of the REE quantity.

(VII) *Insoluble REEs*. The remaining residue was then washed twice with ultrapure water, dried overnight at 105 °C, and ground to fine powder using a rotary disk mill. It was then dissolved completely to allow analysis of the REE content.

All the centrifugal tubes, containers, and flasks used in these processes were soaked in 1 mol L^{-1} HNO_3 for over 24 h and rinsed repeatedly with Milli-Q double de-ionised water (18.25 MΩ cm^{-1}) before use to remove any contaminants. The REE concentrations in the residue and supernatants collected in the processes described above were measured using ICP-MS. The recovery rate of all 7 REE fractions relative to the total REE amount was between 90% and 100% (Table A4).

4. Results

4.1. Mineral components of weathering profile

According to its texture, colour and mineral components, the Renju weathering profile can be divided into four weathering sections–a lateritic horizon (A horizon, 0.0–5.0 m); a completely weathered horizon (B horizon, 5.0–45.0 m) consisting of an upper completely weathered horizon (B1 horizon, 5.0–18.0 m), a feldspar-rich layer (B2 horizon, 18.0–25.0 m), and a lower completely weathered horizon (B3 horizon, 25.0–45.0 m); a semi-weathered horizon (C horizon, 45.0–60.0 m), and fresh bedrock (P horizon, 60.0–78.5 m) (Fig. 2). From top to bottom, the 5 m thick A horizon contains ca. 40% clay minerals and has a brownish red mixed with yellow appearance that gradually turns red near the surface (Fig. 2a). The porous B horizon is approximately 40 m thick, and the B1, B2, and B3 horizons are ca. 13.0 m, ca. 7.0 m, and ca. 20.0 m thick, respectively. The B1 horizon contains more than 60% clay minerals and has a yellow-mottled white appearance (Fig. 2b). The B2 horizon contains more than 60% large particles (0.1–0.5 cm) of quartz and feldspar and has a loose structure and large voids (Fig. 2c). The B3 horizon is brownish-black with a mottled yellow appearance (Fig. 2d) and contains about 60% clay minerals. The C horizon is approximately 22.0 m thick and preserves the texture of granite via some cracks (0.1–10.0 mm) (Fig. 2e). The C horizon has greyish-green appearance due to the extensive chloritisation of biotite and hornblende and the occurrence of clay minerals and red Fe-(hydr)oxides along its cracks and grain boundaries (Fig. 2e). The bedrock is fine-grained (0.5–2.0 mm) equigranular quartz diorite (Fig. 2f) composed mainly of plagioclase, K-feldspar, quartz, biotite, and amphibole; it also includes a small amount of chloritised biotite and amphibole.

4.1.1. Mineral composition

Based on XRD characterisations (Fig. 3; Table A1), the bedrock (i.e. the quartz diorite) beneath the weathered crust consists of plagioclase (53%), amphibole (14%), biotite (10%), chlorite (a hydrothermally

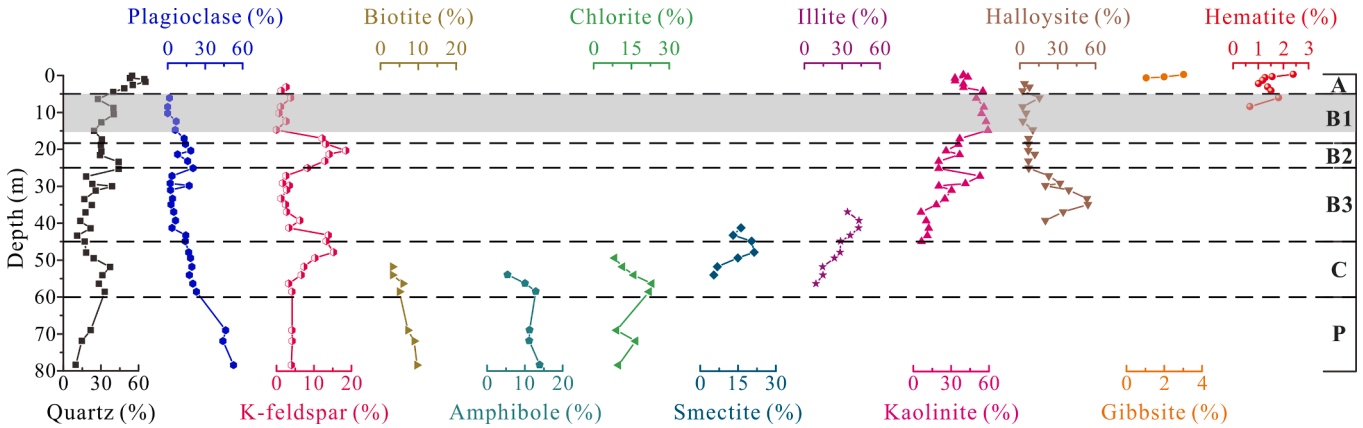

Fig. 3. Variations in content of mineral (quartz, plagioclase, K-feldspar, amphibole, hematite, biotite, chlorite, gibbsite, illite, smectite, halloysite and kaolinite) as a function of depth in the quartz diorite weathering profile. The shaded area represents the REE-rich horizon (at depths of 5.0–15.0 m).

altered product of amphibole and biotite; 10%), quartz (10%), and K-feldspar (4%). The amount of quartz present from the bedrock to the A horizon gradually increases from 10% (at a depth of 78 m) to more than 60% (at a depth of 1 m), while the plagioclase content of gradually decreases from 57% to 0. The presence of K-feldspar is constant, at 4% in the weathering profile, with two exceptionally high occurrences at 13–15% at the upper C and B3 horizons (at depths of 43–48 m) and 13–19% at the B2 horizon (at depths of 18–25 m). Biotite decreases from 10% in the bedrock to<3% in the upper C horizon (at a depth of 52 m). The amphibole content gradually decreases from 14% in the bedrock to 5% in the upper C horizon (at 54 m deep) before disappearing completely. The chlorite concentration increases from 10% at the bedrock to 23% in the upper C horizon (56 m), decreases to 11% in the upper C horizon (at 52 m deep), and also eventually disappears.

With progressive weathering, the primary minerals and hydrothermally altered chlorites gradually transform into secondary minerals including illite, smectite, kaolinite, halloysite, gibbsite, and hematite (Fig. 3). Illite and smectite appear in the upper C horizon. Illite gradually increases up to a maximum content of 43% in the B3 horizon (at 39 m deep), then decreases markedly before eventually disappearing (at a depth of 38 m). Smectite increases up to a maximum content of 21% at the upper C horizon (at 48 m deep) before decreasing rapidly and disappearing in the B3 horizon (at a depth of 39 m). Kaolinite occurs in the upper C horizon (at 45 m deep) and gradually increases up to 53% in the B3 horizon (at a depth of 27 m). Its abundance then decreases abruptly in the B2 horizon (a depths of 18–25 m), followed by a sharp increase from 35% in the upper B2 horizon (at a depth of 18 m) to 60% at the B1 horizon (at 15 m deep) and a gradual decrease from 60% (at a depth of 15 m) to a constant content of 40% in the A horizon. Halloysite appears in the B3 horizon (at a depth of 39 m), and its content rapidly increases to 53% (at 35 m deep) before gradually decreasing to 20% (at 27 m) and then decreasing abruptly to less than 10% in the B2 and A horizons (at depths <25 m). Hematite occurs mainly in the B1 and A horizons (at depths <9 m) and increases upward from 1% to 2%. Gibbsite only occurs in the upper A horizon (at depths <2 m) and increases upwards from 1% to 3%.

4.1.2. Fe-Mn (hydr)oxides

Fe-Mn (hydr)oxides first appear as mineral aggregates, filling the gaps or voids between the minerals in the bedrock (Fig. 4a–b), and occasionally co-existing with cerianite in the C horizon (Fig. 4b). Hematite and goethite are the main Fe (hydr)oxides in weathering crust (Fig. 4c–i). Goethite usually grows as crystals and forms acicular or fibrous particles in the C and lower B horizons (Fig. 4c). The fast Fourier transformation shown in the HRTEM images indicates that the plane distances of the rhombic particles in Fe (hydr)oxides are 0.25 and 0.17 nm, respectively, in accordance with the (1 0 1) and (2 4 0) planes of goethite (Fig. 4g). In the B1 horizon, Fe (hydr)oxides mainly occur as a 'worm structure' with kaolinite or are attached to the surface of laminar kaolinite sheets as globular aggregates (Fig. 4d-4e). In the A horizon, they form aggregates with granulate cerianite in the form of granular hematite and are distributed around laminar kaolinite sheets (Fig. 4f). Granulate cerianite with grain sizes of 5–15 nm are observed in the aggregates as the typical plane distances of 0.31 and 0.19 nm are assigned, respectively, to the (1 1 1) and (2 2 0) planes of cerianite (Fig. 4h). Granulate hematite with grain sizes of 5–20 nm are also observed in the aggregates, with typical plane distances of 0.27 and 0.20 nm assigned to the (1 0 4) and (2 0 2) planes, respectively (Fig. 4i).

4.1.3. REE-bearing minerals

Along the weathering profile, the primary REE-bearing minerals include mainly LREE-rich minerals (e.g. titanite, apatite, allanite, and monazite) and HREE-rich minerals (e.g. xenotime and zircon), while the secondary REE-bearing minerals are deuteric hydrothermal products (i.e. REE fluorocarbonates) and weathering products (e.g. florencite and cerianite). In the bedrock, apatite occurs as spicules or granule inclusions in feldspar and titanite with grain sizes of 30–100 μm (Fig. 5a). The bedrock contains ca. 3% titanite occurring as an anhedral grain sized 200–400 μm (Fig. 5a). Euhedral and subhedral monazite and xenotime are 20–40 μm in size and closely coexist with feldspar and biotite, mostly exhibiting intact morphologies in the bedrock (Fig. 5b). Allanite exists as euhedral grains sized 200–400 μm (Fig. 5c).

A small quantity of fine-grained anhedral REE fluorocarbonate grains (<10 μm) occur in cavities, along grain boundaries, and in cracks between albite and orthoclase (Fig. 5c and 5d) in the bedrock, but disappear in the lower C horizon with progressive weathering. A small quantity of florencite particles sized 1–30 μm also fill the boundaries and voids between apatite and biotite as fine anhedral grains or veins (Fig. 5e) in the C horizon. Titanate and florencite almost disappear in the B3 horizon while apatite is severely weathered, resulting in the formation of plentiful corrosion pits on the surface of the grain (Fig. 5f). Apatite also disappears in the B1 horizon. Most monazite and xenotime is preserved in the B1 and A horizons, with only a few cracks on the surface of the grain, as they form embayed textures during the dissolution along the border of the grain (Fig. 5g and 5 h). Fine-grained cerianite forms spherical aggregates–100–500 nm in size and occurs throughout weathering crust, particularly during oxic weathering of the A horizon (Fig. 5i) that is associated with Fe-Mn (hydr)oxides (Fig. 4a, 4b, and 4f). Zircon is ubiquitous due to its strong resistance to weathering.

4.2. Chemical compositions

4.2.1. Major elements

The bedrock had a relatively homogenous chemical composition of

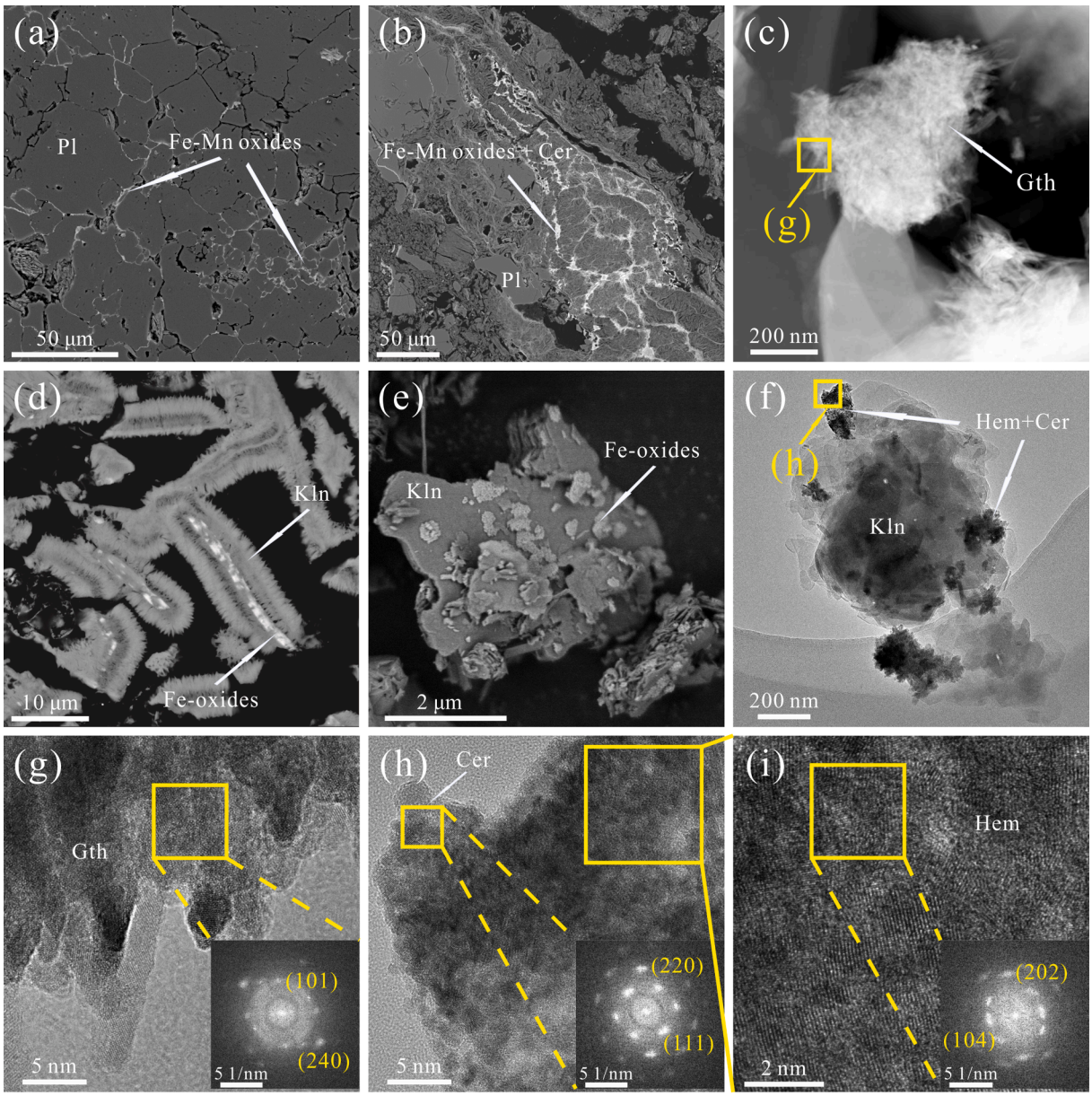

Fig. 4. Scanning electron microscopy (SEM)-backscattered electron images (a, b, d and e) and transmission electron microscopy (TEM) images (c and f-i) of the Fe-Mn (hydr)oxides in the weathered profile of Renju quartz diorite. (a) Fe-Mn oxides filled the gaps in the feldspar particles in the bedrock; (b) Aggregates of Fe-Mn oxides and cerianite filled in the weathering voids in the C horizon; (c) Acicular or fibrous goethite distributed in the upper C horizon and lower B horizon; (d) 'Worm structure' of kaolinite and Fe (hydro)oxides in the B horizon; (e) Globular Fe (hydro)oxides aggregates attached to the surface of laminar kaolinite sheets in the B1 horizon; (f) Aggregates of granular hematite and granulate cerianite distribute around laminar kaolinite sheets in the A horizon; (g) High resolution TEM (HRTEM) images of goethite with fast Fourier transformations from (c); HRTEM images of cerianite (h) and hematite (i) with fast Fourier transformations from (f), and (i) enlarged area of (h). Cer = cerianite; Gth = goethite; Hem = hematite; Kln = kaolinite and Pl = plagioclase.

16.0–17.0 wt% Al_2O_3, 54.8–57.3 wt% SiO_2, 2.94–3.21 wt% Na_2O, 2.30–3.37 wt% K_2O, 6.38–6.65 wt% CaO, 3.27–4.00 wt% MgO, 7.22–8.70 wt% Fe_2O_3, and 0.16–0.19 wt% MnO (Table A2). From the bottom up, the SiO_2 content showed a gradual increasing trend, from 57.3 wt% in the bedrock (at a depth of 78 m) to more than 72.5 wt% in the A horizon (at depths < 5 m) (Fig. 6). The Al_2O_3 content remained stable and varied between 11.1 wt% and 18.8 wt%. However, the K_2O, Na_2O, MgO, and CaO contents gradually decreased from 3.37 wt%, 2.94 wt%, 3.27 wt% and 6.38 wt%, respectively, in the bedrock to 0.79 wt%, 0.04 wt%, 0.21 wt% and 0.03 wt%, respectively, in the upper A horizon (at depths < 1 m). There were slight fluctuations in the Fe_2O_3 and MnO contents that were concentrated mainly in the B1 and A horizons (particularly at 5–15 m); their maxima were 18.8 wt% and 1.68 wt%, respectively.

The chemical evolution of bedrock and weathered crust is intrinsically controlled by the stability of minerals and the mobility of elements during weathering. In this study, the degree of alteration in the weathering profile is estimated using the chemical index of alteration (CIA) (Eq. (1)) (Nesbitt and Young, 1982) as follows:

$$CIA = 100 \times (Al_2O_3/(Al_2O_3 + CaO + Na_2O + K_2O)) \quad (1)$$

The CIA values of bedrock and the C, B, and A horizons are 55–58, 62–65, 65–92, and 94–96, respectively (Fig. 6; Table A2). The CIA values also displayed a gradual increasing trend from 55 in bedrock to 96 in the A horizon; the exception was a slight decrease from 89 at the B3 horizon to 75 at the B2 horizon (at depths of 18–25 m). This indicates an increase in the degree of weathering.

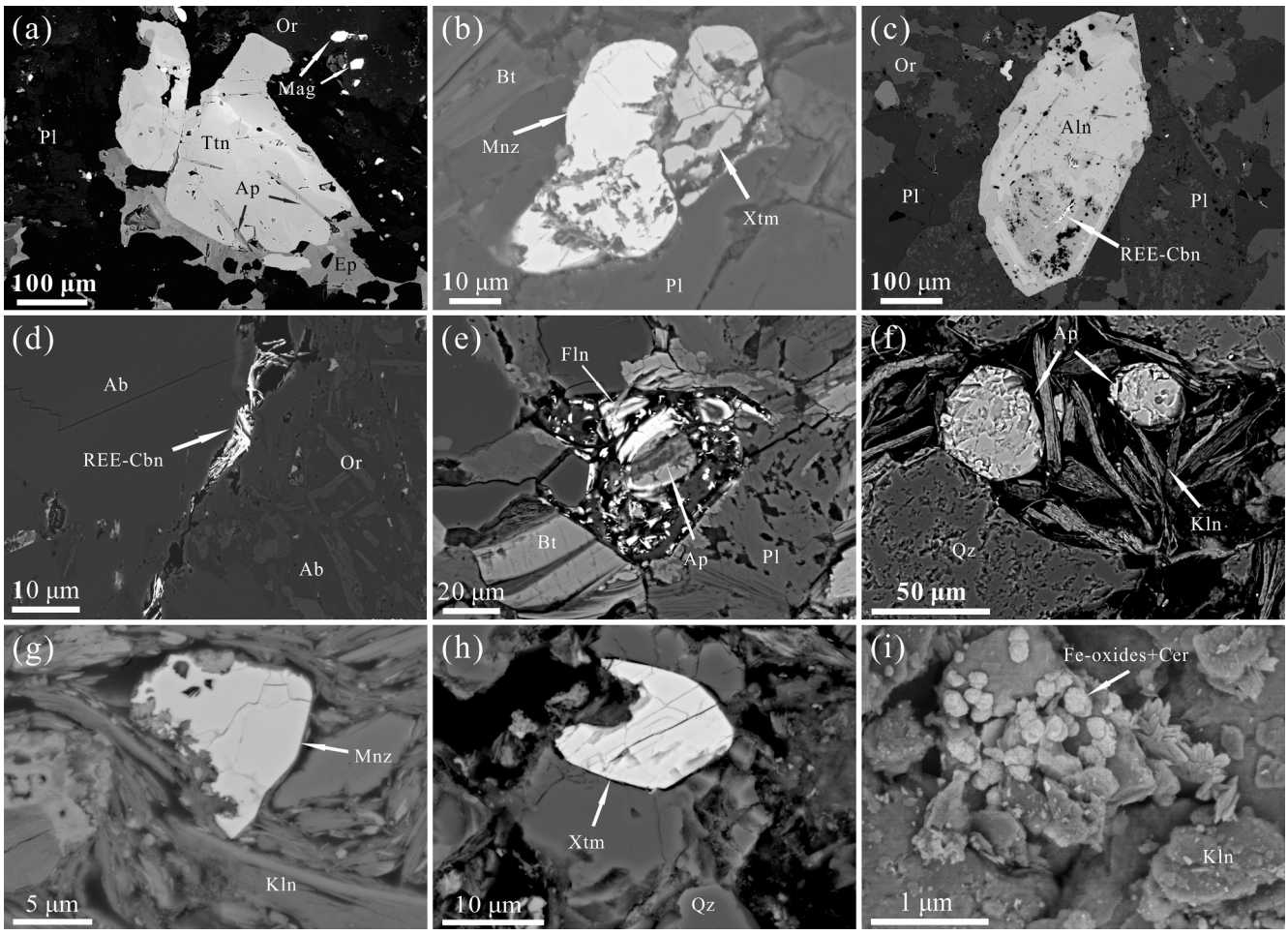

Fig. 5. Scanning electron microscopy (SEM)-backscattered electron images showing the REE-bearing mineral phases in the quartz diorite and weathered quartz diorite studied. (a)-(d) REE-bearing minerals in bedrock; (a) anhedral titanite and acicular apatite; (b) monazite and xenotime adjacent to each other in feldspar and biotite cracks; (c) secondary REE fluorocarbonates in a cavity in original euhedral allanite; (d) REE fluorocarbonate in a crack in perthite; (e)-(f) REE-bearing minerals and secondary REE-bearing minerals in the C horizon; (e) Florencite in apatite and biotite pores; (f) Etch pits on apatite and quartz surfaces; (g)-(h) REE-bearing minerals in the B horizon and A horizon; embayed textures formed by dissolution of (g) residual monazite and (h) residual xenotime; (i) globular aggregate of fine-grained cerianite (CeO_2) with Fe (hydr)oxides. Aln = allanite; Ap = apatite; Bt = biotite; Cer = cerianite; Ep = epidotite; Fln = florencite; Kln = kaolinite; Mag = magnetite; Mnz = monazite; Or = orthoclase; Pl = plagioclase; Qz = quartz; REE-Cbn = REE fluorocarbonate; Ttn = titanite; Xtm = xenotime.

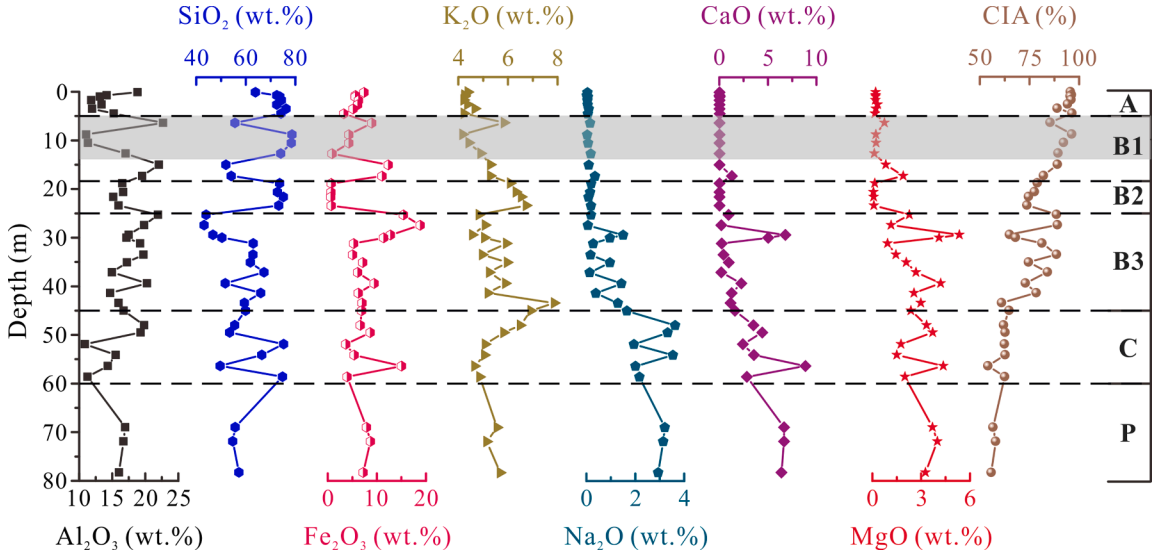

Fig. 6. Variations in major element concentrations and the chemical alteration index (CIA) with depth in the weathering profile of quartz diorite. The shaded area represents the REE-rich horizon (at depths of 5.0–15.0 m).

4.2.2. REE contents

The total REE content in the quartz diorite bedrock ranged from 332 to 338 ppm (Table A3). The chondrite-normalised REE patterns (Fig. 7) show that the bedrock is enriched in LREEs with La/Yb = 26.6 and LREE/HREE = 5.61 and had a slightly negative Ce anomaly (δCe = 0.85). However, the Eu anomaly (δEu = 0.96) was not obvious. The entire regolith displayed a right-inclined REE pattern with obvious Eu negative anomalies; the exception was the B2 horizon (at a depth of 18–25 m) which showed a slightly left-inclined REE pattern. Therefore, the REE fractionation patterns of the weathering profile–with the exception of the Eu anomaly–were identical to those of the bedrock.

From bedrock to the B3 horizon (depths < 33 m), total REE content (ΣREE) was almost constant at 300 ppm, followed by a rapid decrease to a minimum of ca. 113 ppm in the B2 horizon (at depths of 18–25 m) and another subsequent rapid increase to a maximum of ca. 813 ppm in the B1 horizon (at a depth of 6.4 m). REEs are enriched and mineralised (ΣREE > 500 ppm) in the B1 horizon (at depths of 5–15 m) and eventually decreased to less than 300 ppm in the upper A horizon (at depths <4 m) (Fig. 8). The LREE/HREE ratio gradually decreased from bedrock to the B1 horizon (at a depth of 5 m), but increased slightly in the A horizon (at depths <5 m). Apart from an abnormal increase in the B1 horizon (at depths of 33–40 m), the La/Yb ratio displayed a general decrease from 26.6 in the bedrock (at a depth of 78 m) to less than 4.28 in the B2 horizon (at depths of 18–25 m), followed by a gradual increase to 42.5 in the lower A horizon (at a depth of 4.5 m). Eventually, it decreased to 8.55 at the top of the A horizon (at a depth of 0.1 m).

Cerium behaved quite differently from the other REEs. For example, the B and C horizons and the A horizon had negative and positive Ce anomalies of δCe = 0.16–0.87 and δCe = 2.57–4.28, respectively. In contrast, the other REEs were abundant in the B and C horizons, but scarce in the A horizon (Fig. 8). In addition, the variation in the (LREE–Ce)/HREE ratio in the A horizon deviated significantly from that of the LREE/HREE ratio therein, but was highly consistent with that of La/Yb ratio (Fig. 8). Therefore, Ce anomalies accounted for the differences in the variation in the LREE/HREE and La/Yb ratios along the weathering crust.

4.3. REE speciation

Along the weathering profile, REEs were present mainly in the ion exchangeable, residual, and Fe-Mn (hydr)oxide fractions; few REEs existed in the water soluble, carbonate binding, humic acid binding, and strong organic binding fractions (Fig. 9; Table A4).

The water soluble fraction, referring to the REEs that are present as free ions, had an extremely low (<0.01%) concentration in the weathering profile. Thus, its contribution to the total REE content was negligible.

The carbonate binding fraction includes the REEs bonded to carbonate (e.g. REE fluorocarbonate). This fraction increased from 0.4% in the bedrock to 2.3% in the B1 horizon (at a depth of 6 m) before decreasing to 0.5% in the A horizon (at a depth of 4 m) and finally increasing to 4.5% in the upper A horizon (at a depth of 0.1 m) (Fig. 9). The maximum content, 31.4 ppm, appeared in the B1 horizon (at a depth of 15 m) (Fig. A1).

The humic acid binding and strong organic binding fractions refer to the REEs complexed with humic acids (e.g. amino acids and fulvic acids) and organic matter, respectively. Both fractions contributed mostly less than 2% in the weathering profile (Fig. 9). As both fractions were

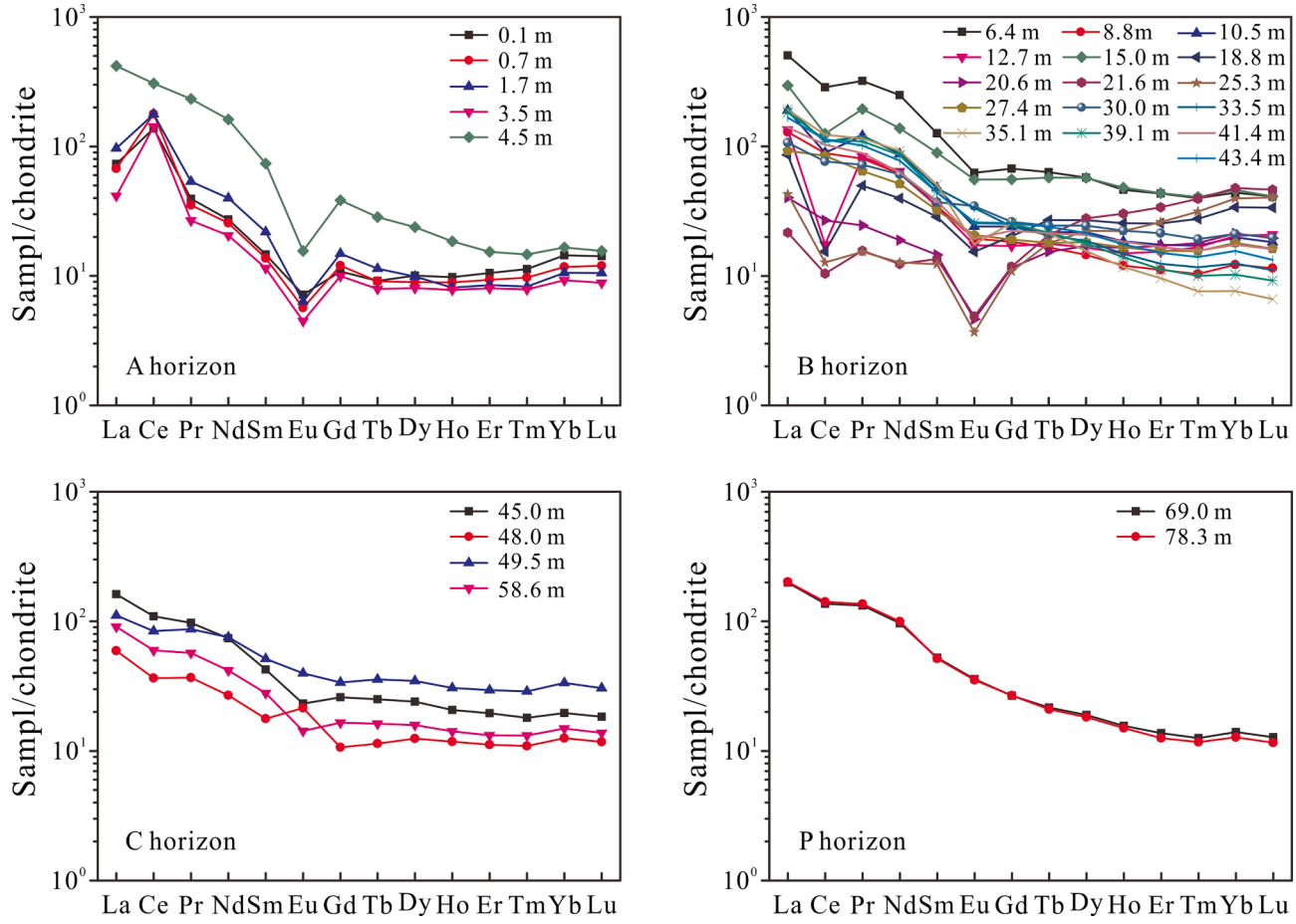

Fig. 7. Chondrite-normalised REE pattern throughout the samples from the regolith (A, B, and C horizons) and the bedrock (P horizon) of the Renju weathering profile. Chondrite values are from McDonough and Sun (1995).

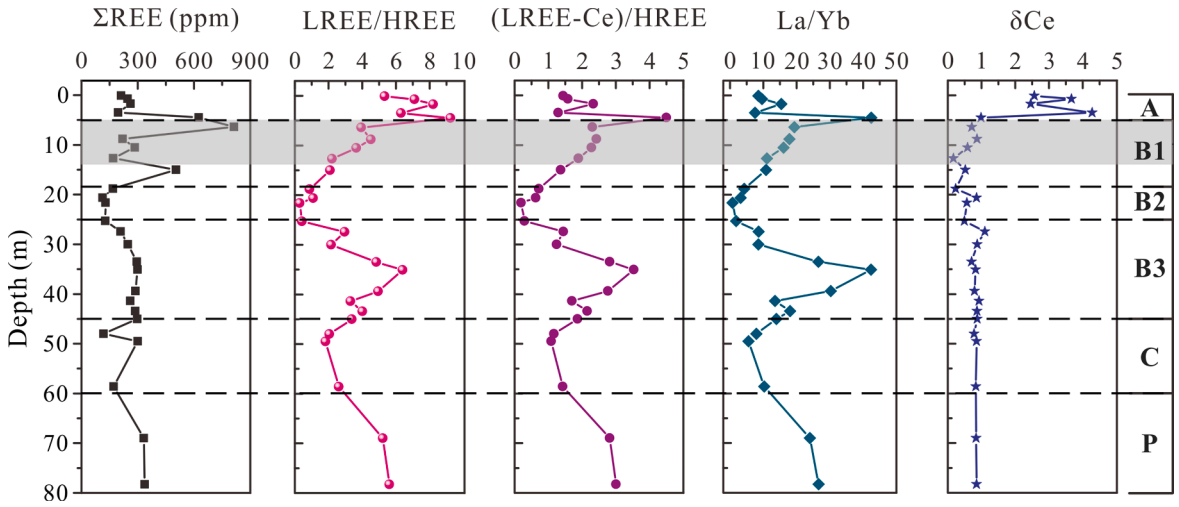

Fig. 8. Variations in concentrations of REEs, LREE/HREE, (LREE–Ce)/HREE, La/Yb, and δCe in bulk samples as a function of depth in the quartz diorite weathering profile. The shaded area represents the REE-rich horizon (at depths of 5.0–15.0 m).

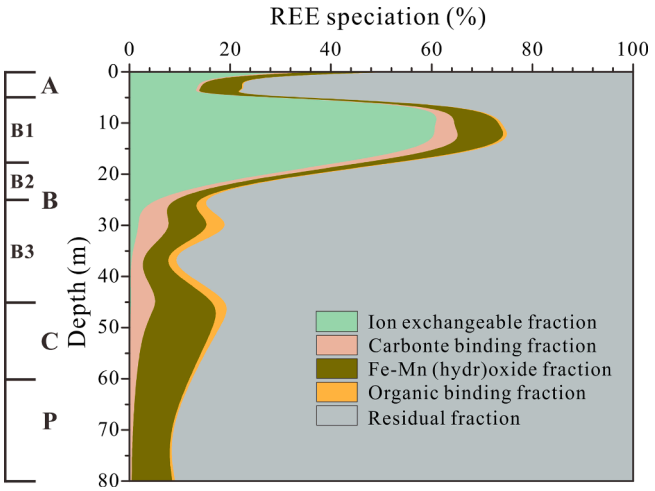

Fig. 9. Variations in REE speciation with depth in the Renju weathering profile.

bonded to organic matter, they are collectively referred to as the 'organic binding fraction' in the following discussion. The concentration of this fraction fluctuated slightly in the weathering profile, where the maximum appeared to be 4.9% in the B3 horizon (ca. 11.7 ppm, at depths of 25–30 m) (Figs. 9 and A1). In addition, the organic binding fraction showed a gradually increasing trend from the bottom to the top of the A horizon. However, the contribution of the organic binding fraction was minor (Fig. 9).

The ion exchangeable fraction represents REEs that are mainly adsorbed by clay minerals and can be exchanged with other cations. It is the main REE speciation needed for the exploitation and utilisation of regolith-hosted REE deposits. From the bedrock to the A horizon, this concentration of this fraction increased slowly to 1.8% (ΣREE, 2.1 ppm) in the lower B2 horizon (at a depth of 25 m) and then increased rapidly to 59.4–66.7% (ΣREE, 312–561 ppm) in the B1 horizon (at depths of 5–15 m). Following this, it decreased sharply to 12.3% (ΣREE, 74.2 ppm) in the lower A horizon (at a depth of 4.5 m), but eventually increased gradually from 13.5% (ΣREE, 25.9 ppm, at a depth of 3.5 m) to 31.0% (ΣREE, 61.2 ppm, at a depth of 0.1 m) in the A horizon (Figs. 9 and A1). Overall, there was a rapid increase in the concentration of the ion exchangeable fraction at a depth of 15 m and a marked decrease after a depth of 5 m, resulting in significant enrichment at depths of 5–15 m (Fig. A1).

The Fe-Mn (hydr)oxide fraction involves REEs bonded to Fe-Mn (hydr)oxides. This fraction increased slightly from 8.2% (ΣREE, 27.1 ppm) at the bedrock to 11.4% (ΣREE, 40.7 ppm) in the C horizon (at a depth of 45 m) and then decreased to 4.4% (ΣREE, 4.6 ppm) in the B2 horizon (at a depth of 20 m). It then quickly increased to 8.0–10.1% (ΣREE, 32.4–40.1 ppm) in the B1 horizon (at depths of 5–15 m) before increasing from 5.4% (ΣREE, 17.8 ppm, at a depth of 4 m) to 15.1% (ΣREE, 29.7 ppm, at a depth of 0.1 m) in the A horizon (Figs. 9 and A1). Overall, the Fe-Mn (hydr)oxide fraction was enriched mainly in the upper C horizon, B3 horizon, and B1 horizon (Fig. A1).

The residual fraction refers to the REEs contained in REE-bearing and rock-forming minerals that were stable during the weathering process. The residual fraction had a constant content of ca. 90% (ΣREE, 110–304 ppm) below the B2 horizon (at depths < 25 m) with only slight fluctuations, followed by a rapid decrease to a minimum of 22.4%–26.8% (ΣREE, 70.2–183 ppm) in the B1 horizon (at depths of 5–15 m). It subsequently increased sharply to 81.7% (ΣREE, 494 ppm) in the lower A horizon (at a depth of 4.5 m) and eventually decreased to 48.8% (ΣREE, 96.2 ppm) in the upper A horizon (at depths < 0.1 m) (Figs. 9 and A1).

5. Discussion

During weathering process, the main factors controlling REE fractionation include preferential dissolution of the primary REE-bearing minerals, complexation with organic and inorganic ligands, and immobilisation through adsorption and precipitation by secondary minerals.

5.1. REE fractionation during dissolution of primary REE-bearing minerals

During weathering of igneous rocks, REE fractionation is strongly dependent on stability and composition of the primary REE-bearing minerals and formation of secondary minerals (Harlavan and Erel, 2002; Li et al., 2019; Nesbitt, 1979; Sanematsu et al., 2016; Stille et al., 2009; Yusoff et al., 2013). For example, several weathering profiles are enriched in HREEs, compared to bedrock, due to dissolution of HREE-bearing minerals (e.g., synchysite-(Y), gadolinite-(Y), and yttrialite-(Y)) (Bao and Zhao, 2008; Li et al., 2019). In contrast, weathering crust can become enriched in LREEs relative to the bedrock while the dissolved REE minerals are dominantly LREE-rich allanite, bastnaesite, and parasite (Estrade et al., 2019; Sanematsu et al., 2013).

In the bedrock of the Renju weathering profile, chondrite-normalised

REE pattern shows an obvious right-inclined style with LREE enrichment (Fig. 7). The bedrock was composed mainly of feldspar, quartz, biotite, and amphibole (Fig. 3) while the dominant REE-bearing minerals were titanite, allanite, REE fluorocarbonate, and apatite accompanied by monazite, xenotime, and zircon (Fig. 5). Among them, most easily weathered minerals are relatively rich in LREEs; examples of the former include titanite (LREE/HREE = 4.42–24.0), allanite (LREE/HREE = 43.8–57.1), REE fluorocarbonate (LREE/HREE = 25.8–33.1), apatite (LREE/HREE = 3.79–37.5), feldspar (LREE/HREE = 8.12–20.1), and biotite (LREE/HREE = 6.75–44.4) (Berger et al., 2014; Condie et al., 1995; Fu et al., 2019; Jiang et al., 2016). All of these completely decomposed below the A horizon (Fig. 5). In contrast, weathering-resistant minerals such as xenotime and zircon are rich in HREEs (LREE/HREE $\leq$ 0.01) (Cetiner et al., 2005; Condie et al., 1995; Fu et al., 2019) and were well preserved in the A horizon after prolonged weathering and leaching (Fig. 5g and h).

In the completely weathered horizon, the rapid decrease in the residual fraction of REEs (Fig. 9) indicated that the easily weathered minerals decomposed markedly under weakly acidic conditions in the weathering crust. These minerals are relatively rich in LREEs; therefore, release and migration of LREEs was more facile than those of HREEs. Thus, the La/Yb ratios showed a decreasing trend from the bedrock to the A horizon (Fig. 8). Moreover, given that the dissolution of REE-bearing minerals depleted the LREEs in the bulk sample–with the exception of weathering-resistant monazite [(LREE)PO_4], which is locally rich in some samples–the La/Yb ratio of the residual fraction was lower than that of the bedrock and decreased with weathering (Fig. 10).

5.2. REE fractionation in mineralisation

In regolith-hosted REE deposits, the fractionation characteristics of REE speciation are greatly affected by those of the bedrock. For example, in the Darongshan weathering crust that developed on LREE-enriched parent granite, the chondrite-normalised REE patterns of Fe-Mn (hydr) oxide fraction showed LREE enrichment (Fu et al., 2019). In contrast, in the Zudong weathering crust that developed on HREE-enriched parent granite, the chondrite-normalised REE patterns of Fe-Mn (hydr)oxide fraction displayed HREE enrichment (Li et al., 2019). Therefore, the fractionation characteristics of REE speciation cannot be normalised simply according to the REE pattern of chondrite; instead, it should be compared to that of the bedrock. This can eliminate the interference from the REE source and highlight the nature of the REE speciation.

During weathering, the decomposition of REE-bearing minerals was accompanied by the conversion of rock-forming minerals such as feldspar, biotite, and amphibole to clay minerals and Fe (hydr)oxides, such as smectite, illite, kaolinite, halloysite, gibbsite, goethite, and hematite (Figs. 3 and 4). The breakdown of rock-forming minerals was documented by the marked drop in the K_2O, Na_2O, MgO, and CaO contents, from 3.37 wt%, 2.94 wt%, 3.27 wt%, and 6.38 wt% in the bedrock, respectively, to 0.79 wt%, 0.04 wt%, 0.21 wt%, and 0.03 wt% in the upper A horizon (Fig. 6). In addition, REEs are released and concentrated in the profile as the ion exchangeable and Fe-Mn (hydr)oxide fractions, with a low quantity in the carbonate and organic binding fractions (Fig. 9). Owing to the variations in environmental conditions and the chemical properties of REEs, REE fractionation takes place during the weathering process.

5.2.1. REE fractionation of the ion exchangeable fraction

The ion exchangeable REEs are the most economically valuable species to exploit. The clay minerals in a regolith include smectite, illite, kaolinite, halloysite and gibbsite; however, kaolinite and halloysite are the primary materials that adsorb REEs (Bao and Zhao, 2008; Borst et al., 2020; Hirst et al., 2017; Li and Zhou, 2020; Sanematsu et al., 2013). The pH of weathering crust ranged from 4 to 7 (Sanematsu and Watanabe, 2016), while the points of zero charge (pH_{pzc}) of kaolinite, illite, and smectite were <3.7, 2.5, and 7–9, respectively (Hirst et al., 2017). Thus, compared to smectite with a positive charge at edge sites, kaolinite and illite with negative changes therein have a higher affinity towards REEs (Sinitsyn et al., 2000). Moreover, illite and smectite mainly occur in the C horizon, from where the REEs could not be leached (Li and Zhou, 2020). This meant that illite and smectite contributed little to REE enrichment in the weathering crust.

In the regolith, REEs are dominantly adsorbed onto kaolinite and halloysite as easily leachable 8- to 9-coordinated outer-sphere hydrated complexes (Borst et al., 2020). The adsorption capacity of both clays increased with the pH level (Yang et al., 2019). In the ion exchangeable fraction, REEs showed LREE/HREE fractionation with LREE enrichment. This resulted in higher La/Yb values (32.7–1618.0) in the ion exchangeable fraction compared to those in the bedrock (26.6) (Fig. 11). Above the REE-rich horizon, the La/Yb ratio in the ion exchangeable fraction gradually decreased (Fig. 11). This suggested that, compared to LREEs, exchangeable HREEs tend to migrate downward with a leaching

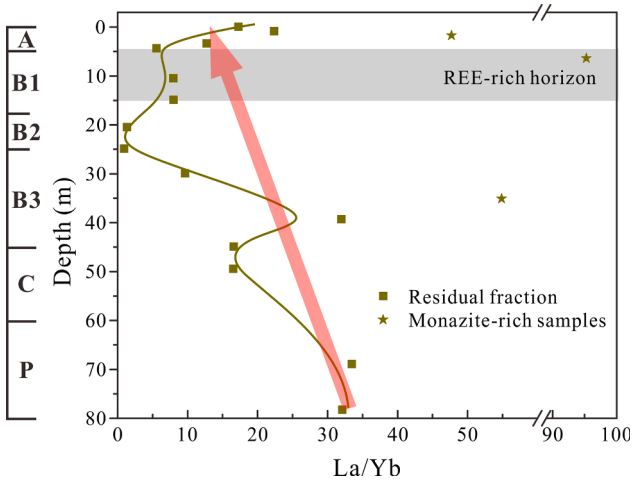

Fig. 10. Variations in the La/Yb ratio of the residual fraction (dark yellow squares) in bulk samples as a function of depth in the Renju weathering profile. High La/Yb values were found in some samples rich in monazite (dark yellow pentacle). The La/Yb ratio of residual fraction decreased gradually with as the degree of weathering (light red arrow) increased.The shaded area represents the REE-rich horizon (at depths of 5.0–15.0 m).

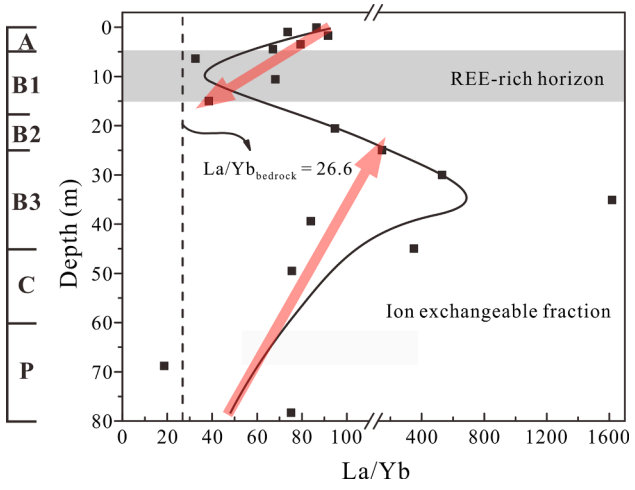

Fig. 11. Variations in the La/Yb ratio of the ion exchangeable fraction (black squares) in bulk samples as a function of depth in the Renju weathering profile. The light red arrow represents the changing trend in the La/Yb ratio of the ion exchangeable fraction. The dashed line represents the La/Yb ratio of the bedrock (La/Yb = 26.6), and the shaded area represents the REE-rich horizon (at depths of 5.0–15.0 m).

fluid. In contrast, exchangeable LREEs and HREEs tended to fractionate at extremely low ΣREE levels in the ion exchangeable fraction (Fig. 11) as their concentrations increased abnormally from the bedrock to the B3 horizon (Fig. A2). However, the adsorption experiments demonstrated that REE adsorption on kaolinite and halloysite only showed weak fractionation when ionic strength and pH were low (ionic strength 0.01–0.025 M; pH = 3.0–6.0) (Coppin et al., 2002; Yang et al., 2019). Thus, the significant LREE/HREE fractionation in the ion exchangeable fraction was probably affected by the speciation of other REEs.

5.2.2. REE fractionation of the Fe-Mn (hydr)oxide fraction

Fe-Mn (hydr)oxides, particularly Fe (hydr)oxides, are ubiquitous in oxic to sub-oxic (near-)surface environments, such as soils, sediments, seawater, and fresh water (Bolanz et al., 2018; Liu et al., 2017). They usually occur as discrete grains, colloidal particles, and coatings on other minerals (Bau, 1999; Li et al., 2017a). Due to their large surface areas and abundant surface hydroxyl groups, they are effective scavengers of metal ions and thus impose an important control on the transfer and fate of metals in supergene environments (Duzgoren-Aydin and Aydin, 2009; Liu et al., 2017). However, studies on the controls of Fe-Mn (hydr)oxides on REE fractionation in regolith-hosted REE deposits of economic importance are quite scarce.

At the onset of weathering, Fe is released from primary Fe oxide minerals (e.g. magnetite and ilmenite) and Fe-bearing silicate minerals (e.g. biotite and amphibole) (Fig. 5a, 5b, and 5e) while Mn present as a trace element in Fe oxides usually leaches with the latter. The released Fe and Mn subsequently form Fe-Mn (hydr)oxides via oxidation and precipitation (Fig. 4a and 4b). Nanocrystalline ferrihydrite ($Fe_{10}O_{14}(OH)_2{\cdot}nH_2O$) is the intermediate product in most cases; it then transforms into thermodynamically stable Fe (hydr)oxides (Barrón and Torrent, 2013; Cornell and Schwertmann, 2003). In the Renju weathering profile, ferrihydrite is transformed into goethite (α-FeOOH) in the C and lower B horizons through dissolution and reprecipitation (Fig. 4c and 4 g). Goethite is then further transformed into hematite (α-Fe_2O_3) in the B1 and A horizons via aggregation, dehydration, and structural rearrangement (Fig. 4f and 4i) (Barrón and Torrent, 2013; Horváth et al., 2000; Cornell and Schwertmann, 2003).

Sequential extraction analysis (Fig. 9) shows that the Fe-Mn (hydr) oxide fraction plays an important role in REE enrichment. In a REE-rich horizon, this fraction makes up 15.9% (i.e. 40.7 ppm) of bulk samples; among the REE fractions, this is less only than the ion exchangeable fraction. The presence of a high concentration of leaching REE cations facilitates adsorption of Fe-Mn (hydr)oxide on the relatively low content. The REE content of the Fe-Mn (hydr)oxide fraction shows a decreasing trend from the bedrock to the bottom of REE-rich horizons (Fig. A1); this is the same as the variations in the Fe_2O_3 and MnO contents (Fig. 6; Table A2). In the bedrock, Fe-Mn (hydr)oxides are generated prior to clay minerals and are well distributed in mineral fractures (Fig. 4a). At the near-neutral pH of bedrock, REEs are probably adsorbed or enter the structure of Fe-Mn (hydr)oxides via co-precipitation (Bolanz et al., 2018; Li et al., 2019).

Fe-Mn (hydr)oxides not only enrich REEs, but also cause the fractionations. The La/Yb ratio of the Fe-Mn (hydr)oxide fraction ranges from 0.57 to 23.3 in all parts of the weathering crust except the upper A horizon, and the latter is at levels generally lower than that in the bedrock (La/Yb = 26.6) (Fig. 12). This indicates that HREEs are selectively enriched in the Fe-Mn (hydr)oxide fraction. This phenomenon agreed with the results of the adsorption experiments and theoretical calculations. The adsorption of REEs on Fe-Mn (hydr)oxides occurs via inner-sphere complexation. Under weakly acidic (pH = 6.1) conditions, HREEs are preferentially enriched in Fe (hydr)oxides (Quinn et al., 2006). This is because HREEs have a smaller ionic radius and stronger hydrolysis ability compared with LREEs and thus have a higher affinity towards Fe (hydr)oxides (Quinn et al., 2006). Moreover, an analysis of the linear free energy relationship conducted by Liu et al. (2017) showed that the estimated equilibrium surface complexation constants increased

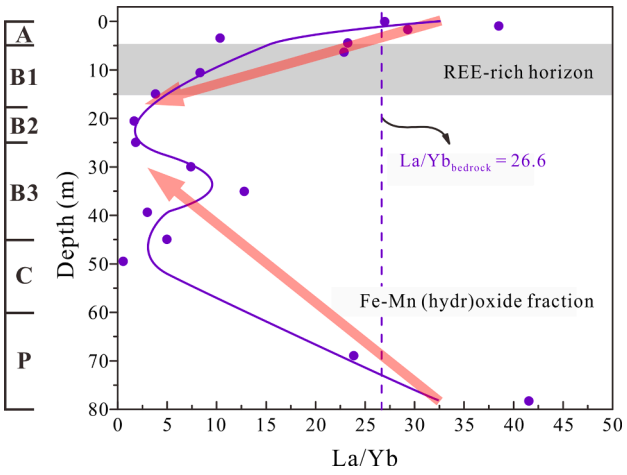

Fig. 12. Variations in the La/Yb ratio of Fe-Mn (hydr)oxide fraction (purple circle) in bulk samples as a function of depth in the Renju weathering profile. The light red arrow represents the changing trend of the La/Yb ratio of Fe-Mn (hydr)oxide fraction. The dashed line represents the La/Yb ratio of the bedrock (La/Yb = 26.6) and the shaded area represents the REE-rich horizon (at depths of 5.0–15.0 m).

from LREEs to HREEs. Therefore, although the REE content in Fe-Mn (hydr)oxide fraction is less than that in the ion exchangeable fraction (Fig. 9), Fe-Mn (hydr)oxides cause significant REE fractionation (Fig. 12). Fe-Mn (hydr)oxides also play a vital role in enrichment of HREEs in the weathering crust, considering that clay minerals cannot lead to REE fractionation.

The La/Yb ratio of the Fe-Mn (hydr)oxide fraction decreased gradually from the A to B1 horizons, with the latter being where the REEs were enriched (Fig. 12). This verified that HREEs tended to migrate with leaching fluid, downwards along the weathering crust, when compared to LREEs. However, they presented a gradual decreasing trend from the bedrock to the B2 horizon. During the initial weathering stage, the most easily weathered minerals–including fluorocarbonates, titanite, and allanite–decomposed first (Fig. 5a, 5c, and 5d). As these minerals were relatively rich in LREEs, any released LREEs were immobilised by Fe-Mn (hydr)oxides, which promoted the enrichment of LREEs in the Fe-Mn (hydr)oxides in the bedrock. HREEs were subsequently leached as weathering proceeded, thereby leading to a gradual decrease in the La/Yb ratio of the Fe-Mn (hydr)oxide fraction.

Finally, owing to the oxidation of Ce^{3+} to form cerianite in the superficial environment, a significant positive Ce anomaly (δCe greater than 1) was found in the Fe-Mn (hydr)oxide fraction; this anomaly increased from the bedrock to the A horizon (Fig. 13). Previous studies on marine Mn deposits suggested that Ce^{3+} could be oxidised by MnO_2 and/or Fe hydroxides to form cerianite (Bau, 1999; Davranche et al., 2008; Koeppenkastrop and Decarlo, 1992). According to TEM and SEM observations of the regolith examined in this study, cerianite coexists closely with Fe-Mn (hydr)oxides in the A horizon (Fig. 4b, 4f, 4h, and 5i). This verified the oxidation of Ce by Fe-Mn (hydr)oxides. Interestingly, a prominent positive Gd anomaly appears in Fe-Mn (hydr)oxides in the A and B horizons (Fig. 13). As the stability constants of Gd complexed with organic ligands were lower than those of neighbouring REEs (Ma et al., 2007), Gd was less likely to have been transferred by leaching fluid and preferentially immobilised by Fe-Mn (hydr)oxides.

5.2.3. REE fractionation of the carbonate binding fraction

(Bi)carbonate complexes were more abundant in the regolith than other inorganic complexes such as SO_4^{2-}, Cl^-, and F^- (Cantrell and Byrne, 1987; Wood, 1990). In the Renju weathering crust, the carbonate binding fraction was concentrated in the B horizon (Fig. 9). This indicated that REEs were primarily complexed with (bi)carbonate ions in

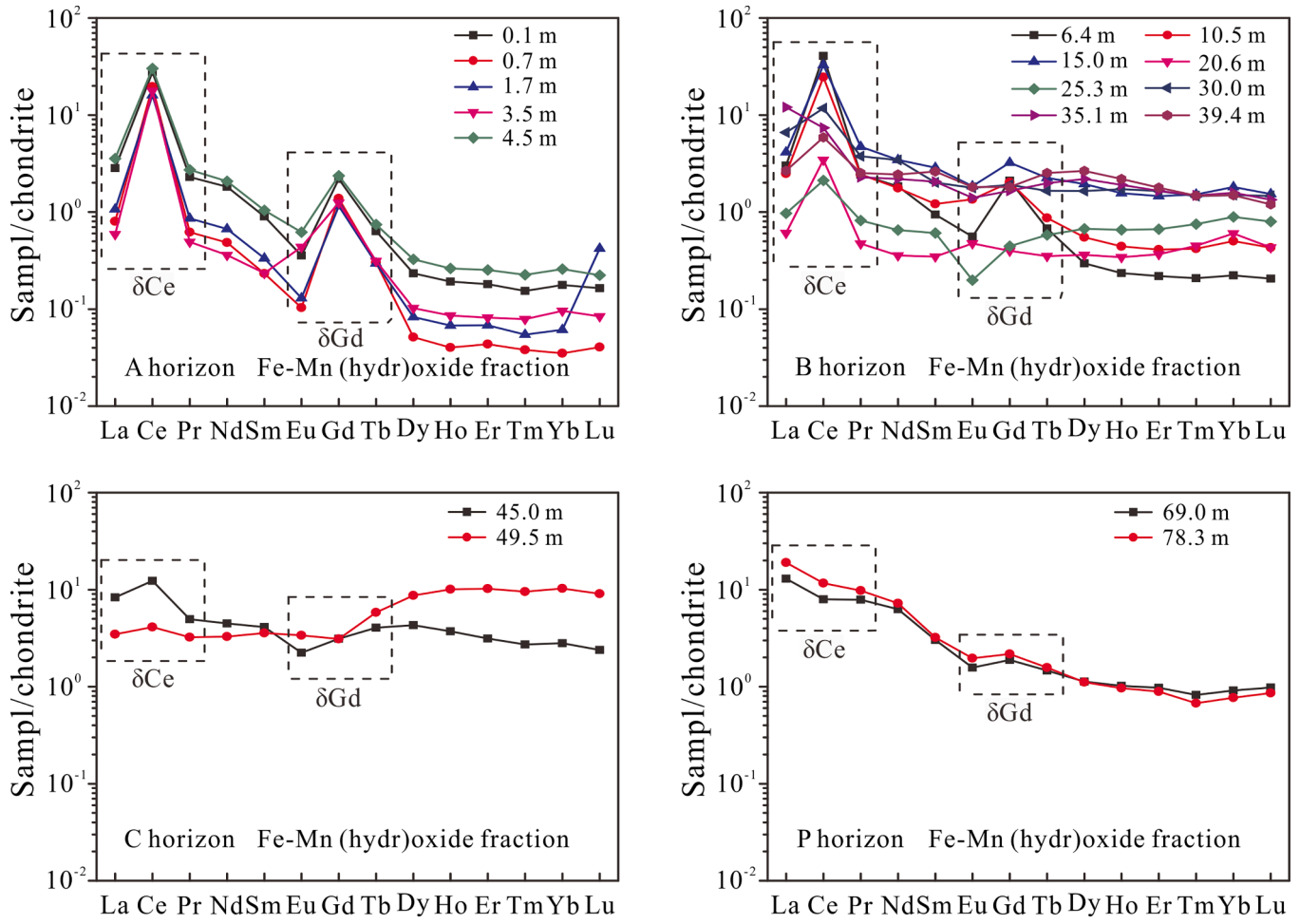

Fig. 13. Chondrite-normalised REE patterns, δCe, and δGd (McDonough and Sun, 1995) of all Fe-Mn (hydr)oxide fractions in the regolith (A, B, and C horizons) and the bedrock (P horizon).

slightly acidic fluids with pH values ranging from 5 to 7 (Liu and Byrne, 1998; Wood, 1990). In the carbonate binding fraction, the La/Yb ratio (1.28–24.1) was mostly lower than that of the bedrock (26.6) (Fig. 14a); thus, HREEs were more easily complexed by (bi)carbonates than LREEs were, consistent with the results of previous simulation experiments (Lee and Byrne, 1993; Luo and Byrne, 2004; Pourret et al., 2007a). As reported in a previous study (Lee and Byrne, 1993), HREEs have a stronger ability to bind to (bi)carbonates because the constant stability of the latter increases from La to Lu. However, in this study several samples showed LREE enrichment in the carbonate binding fraction (Fig. 14a); this was probably due to the presence of secondary LREE minerals, e.g. REE fluorocarbonate (Fig. 5c and 5d).

Along the weathering profile, the variation in the La/Yb ratio of the carbonate binding fraction was similar to that of the Fe-Mn (hydr)oxide fraction. For example, the former showed a gradually decreasing trend from the bedrock to the B2 horizon (Fig. 14a), due to the preferential decomposition of LREE-rich minerals during the initial weathering stage. However, it gradually increased from the B1 to the A horizons, with the reason for this ascribed to the fact that HREEs more easily migrate downward with leaching fluid compared to LREEs.

5.2.4. *REE fractionation of the organic binding fraction*

Organic matter, such as humic and fulvic acids, are critical ligands for complexing REEs during granite weathering (Bao and Zhao, 2008; Pourret et al., 2007b). In the Renju weathering crust, the REE content of the organic binding fraction presented an increasing trend from the A to C horizons (Fig. 9). Based on calculations of thermodynamics, the carboxyl group of humic acid is considered the main binding site for REEs (Pourret et al., 2007a, 2007b; Takahashi et al., 1997). An increase in pH deprotonated the carboxylic groups and promoted the electrostatic attraction between REEs and carboxyl groups (Fairhurst et al., 1995; Lippold et al., 2005), thereby enhancing the REEs bonded to organic matter (Pourret et al., 2007a, 2007b; Sonke and Salters, 2006). The La/Yb ratio of the organic binding fraction (4.50–18.2) was lower than that of the bedrock (La/Yb = 26.6) (Fig. 14b). This was ascribed to the stronger ability of HREEs to bind organic matter relative to LREEs as the bond between REEs and organic matter stabilised with as the ionic radii decreased from La to Lu (Sonke and Salters, 2006; Takahashi et al., 1997). Similar observations have been reported in experimental studies; HREEs have been found to be more strongly bonded to humic substances than LREEs (Wan and Liu, 2006). Moreover, the trend in the variation of the La/Yb ratio of the organic binding fraction along the weathering crust is also analogous to that of the Fe-Mn (hydr)oxide fraction. The former decreased from the A to the B1 horizons but gradually increased from the B2 horizon to the bedrock (Fig. 14b). The reason for such variation has been discussed in the previous Sections 5.2.2 and 5.2.3 on REE fractionation of the Fe-Mn (hydr)oxide and carbonate binding fractions.

5.3. *The mutual effect of REE speciation on REE fractionation*

In the Renju weathering profile, the regolith samples were shown to have inherited the REE patterns of the bedrock, displaying a right-inclined REE pattern (Fig. 7) that is quite close to that of LREE-

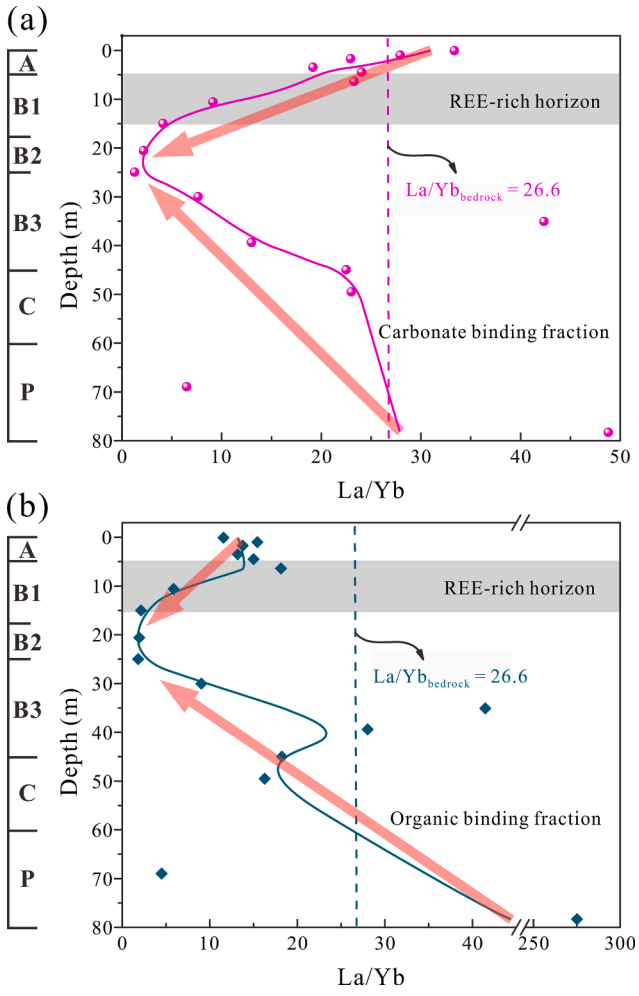

Fig. 14. Variations in the La/Yb ratio of the carbonate and organic binding fractions in bulk samples as a function of depth in the Renju weathering profile. **a.** Variations in the La/Yb ratio (magenta circle) of the carbonate binding fraction. **b.** Organic binding fraction (dark cyan rhombus) as a function of depth in the Renju weathering profile. The light red arrow represents the changing trend of the La/Yb ratio. The dashed line represents the La/Yb ratio of the bedrock (La/Yb = 26.64), and the shaded area represents the REE-rich horizon (at depths of 5.0–15.0 m).

enriched bedrock. However, the REE fractionation is distinct for each type of speciation.

The ion exchangeable fraction of REEs are the main species that are exploited and utilised and considered to have only a weak theoretical REE fractionation (Coppin et al., 2002; Yang et al., 2019). However, this fraction shows obvious LREE enrichment in the weathering crust (Fig. 11). Under incipient weathering, LREE-rich minerals such as REE fluorocarbonate, titanite, and allanite are decomposed in advance, thereby providing a highly concentrated source of REEs (Fig. 5a, c, and d). During REE mineralisation, Fe-Mn (hydr)oxides preferentially adsorb HREEs (Fig. 12) via inner-sphere complexation, making LREEs exclusive as ion exchangeable fractions (Fig. 11). Therefore, the La/Yb ratio of the Fe-Mn (hydr)oxide fraction gradually decreased from the bedrock to the B3 horizon (Fig. 12) and led to an increase in the La/Yb ratio of the ion exchangeable fraction (Fig. 11). This indicated that Fe-Mn (hydro) oxides played a key role in REE fractionation in regolith-hosted REE deposits. Moreover, (bi)carbonates–the most abundant inorganic ligand in the weathering crust (Cantrell and Byrne, 1987; Wood, 1990)–selectively complex with HREEs (Fig. 14a) and produce more LREE sources concentrated in the ion exchangeable fraction. However, according to model calculations, REEs are also inclined to be complexed with humic substances rather than (bi)carbonates in natural water at a pH range of 5–8 (Pourret et al., 2007a, 2007b; Tang and Johannesson, 2003). A previous study showed that REE adsorption onto kaolinite decreased with an increase in the concentration of humic acid (Wan and Liu, 2006). Thus, the preferential complexation of HREE by organic matters (Fig. 14b) inhibited the adsorption of HREEs on kaolinite and halloysite, thus enhancing the LREE/HREE fractionation. Nevertheless, the proportions of REEs present in the organic and carbonate binding fractions are relatively low compared to those in the Fe-Mn (hydr)oxide fraction (Fig. 9).

6. Conclusions

In this study based on the examination of a 78 m long weathering profile developed in quartz diorite of the Renju LREE deposit, REE speciations and their effects on REE fractionation were investigated through analyses of REE concentrations in bulk samples, variations in the lithofacies, sequential extraction, and via bulk physical and chemical parameters of the weathering profile. The bedrock with REE concentrations of 332–338 ppm were enriched in LREEs relative to HREEs and displayed a slightly negative Ce anomaly. At the onset of weathering, LREE-rich minerals such as REE fluorocarbonate, titanite, and allanite were dissolved preferentially, releasing the REEs to the weathering fluid. Following this, HREE-rich minerals including xenotime and zircon accumulated gradually, thereby causing a gradual decrease in the La/Yb ratio of bulk samples with progressive weathering.

In the REE-rich horizon, released REEs are absorbed mainly by kaolinite and halloysite, causing the ion exchangeable fraction to account for 59.4–66.7% (312–561 ppm) of the REE content of bulk samples. Fe-Mn (hydr)oxides also played an important role in REE enrichment where the Fe-Mn (hydr)oxide fraction was up to 15.9% (40.7 ppm) of the bulk sample. REE fractionation occurred in each fraction. Most HREEs were preferentially scavenged in the Fe-Mn (hydr) oxide fraction, with a minority retained in the carbonate and organic binding fractions; these three led to LREE enrichment in the ion exchangeable fraction.

Declaration of Competing Interest

The authors declare that they have no known competing financial interests or personal relationships that could have appeared to influence the work reported in this paper.

Acknowledgements

This work was financially supported by the National Key R&D Program of China (Grant No. 2017YFC0602306); Major Project of Basic and Applied Basic Research in Guangdong Province (Grant No. 2019B030302013); Key Deployment Project of Institute of Geology and Geophysics, Chinese Academy of Sciences (Grant No. IGGCAS-201901); Key Project of Guangzhou Science and Technology Plan (Grant No. 201804020037); the National Natural Science Foundation of China (Grant Nos. 41773113, 41702041, and 42022012); and Science and Technology Planning Project of Guangdong Province, China (Grant Nos. 2017GC010578, 2017GC010128, 2020B1212060055, 2017B030314175, and 2020B1515020015). This is contribution No. IS-3016 from GIGCAS.

Appendix A. Supplementary data

Supplementary data to this article can be found online at https://doi.org/10.1016/j.oregeorev.2021.104172.

References

Bao, Z., Zhao, Z., 2008. Geochemistry of mineralization with exchangeable REY in the weathering crusts of granitic rocks in South China. Ore Geol. Rev. 33, 519–535.

Barrón, V., Torrent, J., 2013. Iron, manganese and aluminium oxides and oxyhydroxides. Eur. Mineral. Union Notes Mineral. 14, 297–336.
Bau, M., 1999. Scavenging of dissolved yttrium and rare earths by precipitating iron oxyhydroxide: experimental evidence for Ce oxidation, Y-Ho fractionation, and lanthanide tetrad effect. Geochim. Cosmochim. Acta 63, 67–77.
Berger, A., Gnos, E., Janots, E., Fernandez, A., Giese, J., 2008. Formation and composition of rhabdophane, bastnasite and hydrated thorium minerals during alteration: implications for geochronology and low-temperature processes. Chem. Geol. 254, 238–248.
Berger, A., Janots, E., Gnos, E., Frei, R., Bernier, F., 2014. Rare earth element mineralogy and geochemistry in a laterite profile from Madagascar. Appl. Geochem. 41, 218–228.
Bolanz, R.M., Kiefer, S., Goettlicher, J., Steininger, R., 2018. Hematite (alpha-Fe_2O_3) – a potential Ce^{4+} carrier in red mud. Sci. Total Environ. 622, 849–860.
Borst, A.M., Smith, M.P., Finch, A.A., Estrade, G., Villanova-de-Benavent, C., Nason, P., et al., 2020. Adsorption of rare earth elements in regolith-hosted clay deposits. Nat. Commun. 11.
Braun, J.J., Riotte, J., Battacharya, S., Violette, A., Oliva, P., Prunier, J., et al., 2018. REY-Th-U dynamics in the critical zone: combined influence of reactive bedrock accessory minerals, authigenic phases, and hydrological sorting (Mule Hole Watershed, South India). Geochem. Geophy. Geosy. 19, 1611–1635.
Cantrell, K.J., Byrne, R.H., 1987. Rare-earth element complexation by carbonate and oxalate ions. Geochim. Cosmochim. Acta 51, 597–605.
Cetiner, Z.S., Wood, S.A., Gammons, C.H., 2005. The aqueous geochemistry of the rare earth elements. Part XIV. The solubility of rare earth element phosphates from 23 to 150 degrees C. Chem. Geol. 217, 147–169.
Chen, B.H., Yu, S., 1994. The geological and geochemical characteristics of late Yanshanian granites in Renju-Huangshe area, Pingyuan, Guangdong. Acta Scientiar. Natural. Univers. Sunyatseni 33, 130–133 (in Chinese with English abstract).
Chen, F., Jia, G., Chen, J., 2009. Nitrate sources and watershed denitrification inferred from nitrate dual isotopes in the Beijiang River, south China. Biogeochemistry 94, 163–174.
Condie, K.C., Dengate, J., Cullers, R.L., 1995. Behavior of rare earth elements in a paleoweathering profile on granodiorite in the Front Range, Colorado, USA. Geochim. Cosmochim. Acta 59, 279–294.
Coppin, F., Berger, G., Bauer, A., Castet, S., Loubet, M., 2002. Sorption of lanthanides on smectite and kaolinite. Chem. Geol. 182, 57–68.
Cornell, R.M., Schwertmann, U., 2003. The Iron Oxides: Structure, Properties, Reactions, Occurences and Uses. Wiley-VCH.
Dardenne, K., Schafer, T., Lindqvist-Reis, P., Denecke, M.A., Plaschke, M., Rothe, J., et al., 2002. Low temperature XAFS investigation on the lutetium binding changes during the 2-line ferrihydrite alteration process. Environ. Sci. Technol. 36, 5092–5099.
Davranche, M., Pourret, O., Gruau, G., Dia, A., 2004. Impact of humate complexation on the adsorption of REE onto Fe oxyhydroxide. J. Colloid Interf. Sci. 277, 271–279.
Davranche, M., Pourret, O., Gruau, G., Dia, A., Jin, D., Gaertner, D., 2008. Competitive binding of REE to humic acid and manganese oxide: impact of reaction kinetics on development of cerium anomaly and REE adsorption. Chem. Geol. 247, 154–170.
Duzgoren-Aydin, N.S., Aydin, A., 2009. Distribution of rare earth elements and oxyhydroxide phases within a weathered felsic igneous profile in Hong Kong. J. Asian Earth Sci. 34, 1–9.
Estrade, G., Marquis, E., Smith, M., Goodenough, K., Nason, P., 2019. REE concentration processes in ion adsorption deposits: evidence from the Ambohimirahavavy alkaline complex in Madagascar. Ore Geol. Rev. 112.
Fairhurst, A.J., Warwick, P., Richardson, S., 1995. The Influence of Humic-Acid on the Adsorption of Europium onto Inorganic Colloids as a Function of Ph. Colloids and Surfaces a-Physicochemical and Engineering Aspects 99, 187–199.
Fu, W., Li, X., Feng, Y., Feng, M., Peng, Z., Yu, H., et al., 2019. Chemical weathering of S-type granite and formation of Rare Earth Element (REE)-rich regolith in South China: critical control of lithology. Chem. Geol. 520, 33–51.
GBW07441-074451, 2007. Certified reference materials for element forms in soils. (in Chinese).
Harlavan, Y., Erel, Y., 2002. The release of Pb and REE from granitoids by the dissolution of accessory phases. Geochim. Cosmochim. Acta 66, 837–848.
Hirst, C., Andersson, P.S., Shaw, S., Burke, I.T., Kutscher, L., Murphy, M.J., et al., 2017. Characterisation of Fe-bearing particles and colloids in the Lena River basin, NE Russia. Geochim. Cosmochim. Acta 213, 553–573.
Horváth, Z., Varga, B., Mindszenty, A., 2000. Micromorphological and chemical complexities of a lateritic profile from basalt (Jos Plateau, Central Nigeria). Chem. Geol. 170, 81–93.
Janots, E., Bernier, F., Brunet, F., Munoz, M., Trcera, N., Berger, A., et al., 2015. Ce(III) and Ce(IV) (re)distribution and fractionation in a laterite profile from Madagascar: insights from in situ XANES spectroscopy at the Ce L-III-edge. Geochim. Cosmochim. Acta 153, 134–148.
Jiang, P., Yang, K.-F., Fan, H.-R., Liu, X., Cai, Y.-C., Yang, Y.-H., 2016. Titanite-scale insights into multi-stage magma mixing in Early Cretaceous of NW Jiaodong terrane, North China Craton. Lithos 258, 197–214.
Koeppenkastrop, D., Decarlo, E.H., 1992. Sorption of rare-earth elements from seawater onto synthetic mineral particles: an experimental approach. Chem. Geol. 95, 251–263.
Lara, M.C., Buss, H.L., Pett-Ridge, J.C., 2018. The effects of lithology on trace element and REE behavior during tropical weathering. Chem. Geol. 500, 88–102.
Lee, J.H., Byrne, R.H., 1993. Complexation of trivalent rare-earth elements (Ce, Eu, Gd, Tb, Yb) by carbonate ions. Geochim. Cosmochim. Acta 57, 295–302.
Li, M., Liu, H., Chen, T., Hayat, T., Alharbi, N.S., Chen, C., 2017a. Adsorption of Europium on Al-substituted goethite. J. Mol. Liq. 236, 445–451.
Li, M.Y.H., Zhou, M.-F., 2020. The role of clay minerals in formation of the regolith-hosted heavy rare earth element deposits. Am. Mineral. 105, 92–108.
Li, M.Y.H., Zhou, M.-F., Williams-Jones, A.E., 2019. The genesis of Regolith-hosted heavy rare earth element deposits: insights from the world-Class Zudong Deposit in Jiangxi Province, South China. Econ. Geol. 114, 541–568.
Li, M.Y.H., Zhou, M.-F., Williams-Jones, A.E., 2020. Controls on the dynamics of rare earth elements during subtropical hillslope processes and formation of regolith-hosted deposits. Econ. Geol. 115, 1097–1118.
Li, Y.H.M., Zhao, W.W., Zhou, M.-F., 2017b. Nature of parent rocks, mineralization styles and ore genesis of regolithhosted REE deposits in South China: an integrated genetic model. J. Asian Earth Sci. 148, 65–95.
Liu, H., Pourret, O., Guo, H., Bonhoure, J., 2017. Rare earth elements sorption to iron oxyhydroxide: Model development and application to groundwater. Appl. Geochem. 87, 158–166.
Lippold, H., Muller, N., Kupsch, H., 2005. Effect of humic acid on the pH-dependent adsorption of terbium(III) onto geological materials. Applied Geochemistry 20, 1209–1217.
Liu, X.W., Byrne, R.H., 1998. Comprehensive investigation of yttrium and rare earth element complexation by carbonate ions using ICP mass spectrometry. J. Solution Chem. 27, 803–815.
Luo, Y.R., Byrne, R.H., 2004. Carbonate complexation of yttrium and the rare earth elements in natural waters. Geochim. Cosmochim. Acta 68, 691–699.
Ma, J.-L., Wei, G.-J., Xu, Y.-G., Long, W.-G., Sun, W.-D., 2007. Mobilization and re-distribution of major and trace elements during extreme weathering of basalt in Hainan Island, South China. Geochim. Cosmochim. Acta 71, 3223–3237.
McDonough, W.F., Sun, S.S., 1995. The composition of the Earth. Chem. Geol. 120, 223–253.
Nesbitt, H.W., 1979. Mobility and fractionation of rare earth elements during weathering of a granodiorite. Nature 279, 206–210.
Nesbitt, H.W., Young, G.M., 1982. Early Proterozoic climates and plate motions inferred from major element chemistry of lutites. Nature 299, 715–717.
Piasecki, W., Sverjensky, D.A., 2008. Speciation of adsorbed yttrium and rare earth elements on oxide surfaces. Geochim. Cosmochim. Acta 72, 3964–3979.
Pourret, O., Davranche, M., Gruau, G., Dia, A., 2007a. Competition between humic acid and carbonates for rare earth elements complexation. J. Colloid Interf. Sci. 305, 25–31.
Pourret, O., Davranche, M., Gruau, G., Dia, A., 2007b. Rare earth elements complexation with humic acid. Chem. Geol. 243, 128–141.
Quinn, K.A., Byrne, R.H., Schijf, J., 2006. Sorption of yttrium and rare earth elements by amorphous ferric hydroxide: Influence of pH and ionic strength. Mar. Chem. 99, 128–150.
Ramsey, M.H., Potts, P.J., Webb, P.C., Watkins, P., Watson, J.S., Coles, B.J., 1995. An objective assessment of analytical method precision:comparison of ICP-AES and XRF for the analysis of silicate rocks. Chem. Geol. 124, 1–19.
Regional Geological Survey Team of Jiangxi Geological Burea., 1976. Report of 1: 200,000 regional geological survey of the Xunwu region: Anyuan (in Chinese).
Riesgo Garcia, M.V., Krzemien, A., Manzanedo del Campo, M.A., Menendez Alvarez, M., Richard Gent, M., 2017. Rare earth elements mining investment: it is not all about China. Resour. Policy 53, 66–76.
Sanematsu, K., Ejima, T., Kon, Y., Manaka, T., Zaw, K., Morita, S., et al., 2016. Fractionation of rare-earth elements during magmatic differentiation and weathering of calc-alkaline granites in southern Myanmar. Mineral. Mag. 80, 77–102.
Sanematsu, K., Kon, Y., Imai, A., Watanabe, K., Watanabe, Y., 2013. Geochemical and mineralogical characteristics of ion-adsorption type REE mineralization in Phuket, Thailand. Miner. Deposita 48, 437–451.
Sanematsu, K., Watanabe, Y., 2016. Characteristics and Genesis of Ion Adsorption-Type Rare Earth Element Deposits, in: Verplanck PL, Hitzman MW (Eds.), Rare Earth and Critical Elements in Ore Deposits, pp. 55–79.
Shi, Y., Qiu, L., Tang, B., Yang, Z., Song, C., Gu, X., 2014. Determination of total ionic-phase rare earth and component in ion-adsorption rare earth ore by inductively coupled plasma mass spectrometry. Metall. Anal. 34, 14–19.
Sinitsyn, V.A., Aja, S.U., Kulik, D.A., Wood, S.A., 2000. Acid-base surface chemistry and sorption of some lanthanides on K^+-saturated marblehead illite: I. Results of an experimental investigation. Geochim. Cosmochim. Acta 64, 185–194.
Sonke, J.E., Salters, V.J.M., 2006. Lanthanide-humic substances complexation. I. Experimental evidence for a lanthanide contraction effect. Geochim. Cosmochim. Acta 70, 1495–1506.
Stille, P., Pierret, M.C., Steinmann, M., Chabaux, F., Boutin, R., Aubert, D., et al., 2009. Impact of atmospheric deposition, biogeochemical cycling and water-mineral interaction on REE fractionation in acidic surface soils and soil water (the Strengbach case). Chem. Geol. 264, 173–186.
Takahashi, Y., Minai, Y., Ambe, S., Makide, Y., Ambe, F., Tominaga, T., 1997. Simultaneous determination of stability constants of humate complexes with various metal ions using multitracer technique. Sci. Total Environ. 198, 61–71.
Tang, J., Johannesson, K.H., 2010. Ligand extraction of rare earth elements from aquifer sediments: Implications for rare earth element complexation with organic matter in natural waters. Geochim. Cosmochim. Acta 74, 6690–6705.
Tang, J.W., Johannesson, K.H., 2003. Speciation of rare earth elements in natural terrestrial waters: Assessing the role of dissolved organic matter from the modeling approach. Geochim. Cosmochim. Acta 67, 2321–2339.
Wan, Y., Liu, C., 2006. The effect of humic acid on the adsorption of REEs on kaolin. Colloids Surfaces A 290, 112–117.
Wang, Z., Ma, J., Li, J., Wei, G., Zeng, T., Li, L., et al., 2018. Fe (hydro) oxide controls Mo isotope fractionation during the weathering of granite. Geochim. Cosmochim. Acta 226, 1–17.

Wang, Z.G., Xu, J.H., 2016. Characteristics and prevention measures of soil erosion in Renju rare earth mining area in northern Guangdong province. Subtrop. Soil Water Conserv. 28, 51–56 (in Chinese).
Wood, S.A., 1990. The aqueous geochemistry of the rare-earth elements and yttrium: 1. Review of available low-temperature data for inorganic complexes and the inorganic REE speciation of natural waters. Chem. Geol. 82, 159–186.
Xu, C., Kynicky, J., Smith, M.P., Kopriva, A., Brtnicky, M., Urubek, T., et al., 2017. Origin of heavy rare earth mineralization in South China. Nat. Commun. 8.
Yang, M., Liang, X., Ma, L., Huang, J., He, H., Zhu, J., 2019. Adsorption of REEs on kaolinite and halloysite: a link to the REE distribution on clays in the weathering crust of granite. Chem. Geol. 525, 210–217.
Yu, C.X., Drake, H., Mathurin, F.A., Astrom, M.E., 2017. Cerium sequestration and accumulation in fractured crystalline bedrock: the role of Mn-Fe (hydr-)oxides and clay minerals. Geochim. Cosmochim. Acta 199, 370–389.
Yusoff, Z.M., Ngwenya, B.T., Parsons, I., 2013. Mobility and fractionation of REEs during deep weathering of geochemically contrasting granites in a tropical setting, Malaysia. Chem. Geol. 349, 71–86.
Zhong, Y., Liu, Q., Chen, Z., Javier Gonzalez, F., Hein, J.R., Zhang, J., et al., 2019. Tectonic and paleoceanographic conditions during the formation of ferromanganese nodules from the northern South China Sea based on the high-resolution geochemistry, mineralogy and isotopes. Mar. Geol. 410, 146–163.